



# Liquid plugs in narrow tubes: application to airway occlusion

Georg F. Dietze<sup>†</sup>

Université Paris-Saclay, CNRS, FAST, 91405 Orsay, France

(Received 23 March 2024; revised 17 June 2024; accepted 31 July 2024)

We study liquid plugs in the pulmonary airways based on the two-phase axisymmetric weighted residual integral boundary-layer model of Dietze *et al.* (*J. Fluid Mech.*, vol. 894, 2020, A17), which was originally developed to study liquid films coating the inner surface of a cylindrical tube in interaction with a core gas flow. The augmented form of this model, which was never applied beyond a proof of concept, allows for the representation of liquid pseudo-plugs. Here, we demonstrate its predictive power vs experiments and direct numerical simulations, in terms of the dynamics of plug formation and the characteristics of developed liquid plugs, such as their shape, flow field, speed and length, as well as the associated wall stresses and their spatial derivatives. In particular, we show that the augmented model allows us to establish a direct continuation path from travelling-wave solutions (TWS) to travelling-plug solutions (TPS). We then apply the model to predict mucus plugs in the conducting zone of the tracheobronchial tree, based on the lung architecture model of Weibel. We proceed by numerical continuation of travelling-state solutions in terms of the airway generation, whereby we impose the wavelength of the linearly most-amplified convective instability (CI) mode or that of the absolute instability (AI) mode. We identify the critical airway generation for liquid-plug formation (TWS/TPS transition), maximum potential for wall-stress-induced epithelial cell damage and CI/AI transition, and investigate how these phenomena are affected by the main control parameters, i.e. airway orientation vs gravity, air flow rate, mucus properties and airway size.

**Key words:** thin films, pulmonary fluid mechanics

## 1. Introduction

Liquid plugs forming as a result of the Plateau–Raleigh instability from a liquid film coating the inner surface of a cylindrical tube (figure 1) occur in several applications, e.g. in pulsating heat pipes as a result of phase transition (Nikolayev & Marengo 2018), in concepts for cleaning contaminated surfaces (Zoueshtiagh, Baudoin & Guerrin 2014; Khodaparast *et al.* 2017), in surfactant replacement therapy (SRT), where a surfactant-rich

<sup>†</sup> Email address for correspondence: [georg.dietze@cnrs.fr](mailto:georg.dietze@cnrs.fr)

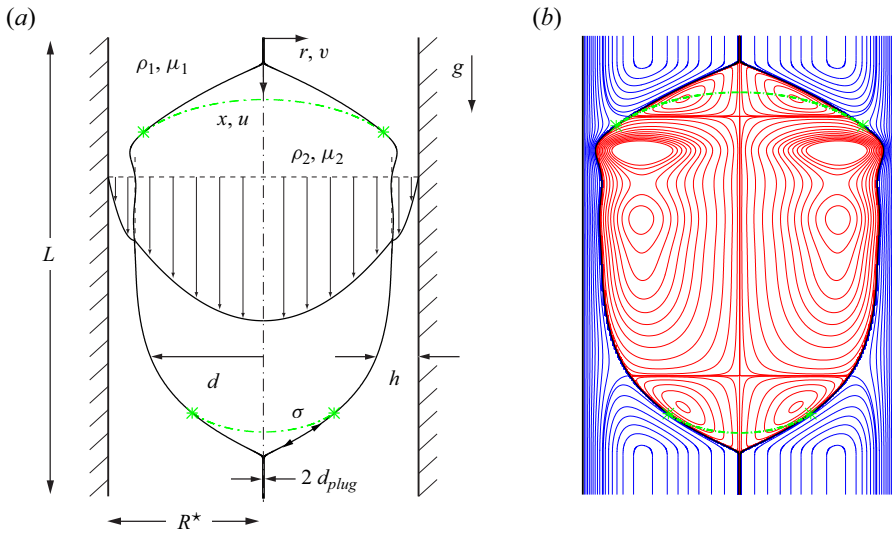


Figure 1. Liquid plugs (subscript 1) enclosing a gas bubble (subscript 2) formed by the occlusion of a narrow cylindrical tube by a falling liquid film lining its inner surface. (a) Problem sketch and notations. The tube radius  $R^*$  is used as the length scale, the star superscript designating dimensional quantities; (b) travelling-state solution obtained from our model (2.13) for a vertical configuration:  $Ka = 121.4$  (silicone oil II in table 1),  $R^* = 1.5$  mm,  $L = \Lambda = 5.4$ ,  $V_1/\pi/R^3 = 2.85$ ,  $M = 1$ ,  $d_{plug} = 0.01$ ,  $Re_1 = 14.6$ ,  $Re_2 = 30.8$ , where  $L$ ,  $\Lambda$ ,  $V_1$ ,  $M$ ,  $d_{plug}$  and  $Re$  denote the domain length, wavelength, liquid volume, normalized gas pressure drop (2.18), pseudo-plug core radius (2.13c) and Reynolds number, respectively. Streamlines in the moving reference frame within the liquid (blue lines) and gas (red lines). Dot-dashed green lines correspond to spherical-cap reconstruction (2.14) between patching points marked by asterisks.

liquid is injected into the lungs (Filoche, Tai & Grotberg 2015), and in airway occlusion (Grotberg 1994, 2011), typically when the mucus film lining the pulmonary airways exceeds the threshold volume for liquid unduloids (Everett & Haynes 1972).

In the current manuscript, we are mainly interested in airway occlusion, where hydrodynamical studies have focused on two key issues: (i) predicting the threshold for liquid-plug formation under increasingly realistic operating conditions, which is essential for designing effective assisted ventilation protocols (Halpern, Jensen & Grotberg 1998); and (ii) predicting the wall stresses associated with liquid plugs, which are known to cause epithelial cell damage (Bilek, Dee & Gaver 2003). We aim to contribute to these tasks by applying the two-phase axisymmetric weighted residual integral boundary-layer (WRIBL) model of Dietze & Ruyer-Quil (2015), which was augmented in Dietze, Lavalle & Ruyer-Quil (2020) for the representation of liquid plugs.

We start by describing the state of the art on the fluid mechanics of liquid plugs, with particular attention to their occurrence in the human lung. The modelling of liquid plugs was initiated by Bretherton (1961), who predicted the shape of a long Taylor bubble (Taylor 1961) propagating in a liquid-filled narrow cylindrical capillary, in the absence of gravity and for a passive gas, i.e.  $\Pi_\mu = \Pi_\rho = 0$ , where  $\Pi_\rho = \rho_2/\rho_1$  and  $\Pi_\mu = \mu_2/\mu_1$  denote the gas/liquid density and dynamic viscosity ratios. This solution was based on the lubrication equations describing the thin liquid film enclosing the gas bubble, which are obtained by truncating the governing equations at order  $\epsilon^0$  in the long-wave parameter,  $\epsilon = h^*/\Lambda^*$  (stars will denote dimensional quantities throughout), which relates the liquid film thickness,  $h^*$ , to the wavelength,  $\Lambda^*$ , of the bubble/plug arrangement (see figure 1). This lubrication solution is matched to two spherical caps at the leading and trailing

ends of the bubble. Subsequent works retained the assumption of inertialess flow, but made technical improvements, such as accounting for the finite thickness of the residual film (Aussillous & Quéré 2000; Klaseboer, Gupta & Manica 2014), or by accounting for higher-order viscous effects, via asymptotic expansions in terms of the capillary number,  $Ca = \mu_1 U_2 / \sigma$ , where  $\mu_1$ ,  $U_2$  and  $\sigma$  denote the liquid dynamic viscosity, the gas superficial velocity and the surface tension, and/or in terms of the long-wave parameter,  $\epsilon$  (Park & Homsy 1984; Jensen *et al.* 1987). Other works accounted for the effect of gravity (Jensen *et al.* 1987; Lasseux 1995; Atasi *et al.* 2017), a contact line at the leading front of the liquid plug (Kalliadasis & Chang 1994; Bico & Quéré 2001) or a flexible tube wall (Howell, Water & Grotberg 2000).

Lubrication models following the above-described approach have been applied to simulate liquid plugs in the pulmonary airways. For example, Suresh & Grotberg (2005) investigated the effect of gravity on the liquid distribution within a liquid plug upstream of an inclined airway bifurcation, in order to quantify the maldistribution into the daughter airways. More recently, Fujioka *et al.* (2016) introduced a three-zone model for long liquid plugs, where the non-interacting leading and trailing menisci were represented via lubrication solutions from the literature (Kalliadasis & Chang 1994; Klaseboer *et al.* 2014). The authors applied their model, which compares favourably with direct numerical simulations (DNS) in regimes with negligible inertia, to study the transient evolution of pressure-driven liquid plugs, leading up to plug rupture. Throughout the manuscript, we will designate numerical simulations based on the full Navier–Stokes equations as DNS, even though these simulations do not concern turbulent flows. The authors also determined correlations for the maximum wall stresses and their spatial derivatives, in order to predict the potential for epithelial cell damage.

When inertia is not negligible, the low-dimensional representation of liquid plugs in cylindrical tubes needs to be extended beyond the lubrication approximation (Heil 2001). For example, Aussillous & Quéré (2000) extended the lubrication solution of Bretherton (1961) based on an empirical approach by incorporating the Weber number, which relates inertia to capillarity. A different approach was followed in Dietze *et al.* (2020), where we introduced an augmented simplified order- $\epsilon^2$  WRIBL model that represents the dynamics of a liquid film coating the inner surface of a cylindrical tube of radius,  $R^*$ , in contact with a core gas flow. A repulsive source term,  $\Pi_\phi$ , which enters the integral momentum equation (2.13a) and which will be defined in § 2 (see (2.13c) there), allows us to stabilize the liquid–gas interface when the core radius,  $d^*$ , becomes very small, i.e.  $d^* = d_{plug}^* \ll R^*$ . The source term becomes noticeable only when the liquid–gas interface evolves toward occluding the tube under the driving effect of the Plateau–Rayleigh instability, and it eventually stabilizes the solution in the form of a pseudo-plug, consisting of a liquid annulus filling almost the entire cross-section of the tube and an arbitrarily thin gas filament at the tube axis. This approach is similar to using a precursor film for simulating contact line problems with thin-film models (Thiele *et al.* 2001). The augmented WRIBL model was introduced in the appendix of Dietze *et al.* (2020), but never applied beyond a proof of concept. In the current manuscript, we validate it vs experiments and DNS and apply it to predict liquid plugs in the pulmonary airways.

Low-dimensional models for liquid plugs have often been used as building blocks in fluid mechanical multi-scale models representing the entire tracheobronchial tree. For example, Halpern *et al.* (1998) modelled the respiratory network by considering that the airway diameter, airway cross-section and ventilation flow rate all vary as continuous functions of the airway generation,  $n$ , according to the lung architecture model of Weibel & Gomez (1962). Using this approach, the authors mimicked SRT by simulating the delivery of surfactant-rich liquid from a liquid plug propagating through the model lung, based

on an inertialess low-dimensional solution for the deposited film thickness. Later, Filoche *et al.* (2015) extended this work by accounting for the gravity-induced maldistribution of liquid at airway bifurcations, and investigated the effect of patient orientation on the effectiveness of SRT protocols. Ryans *et al.* (2016) constructed a multi-scale model of the conducting zone of the tracheobronchial tree ( $n \leq 16$ ) based on the lubrication model of Fujioka *et al.* (2016) for representing liquid plugs. This multi-scale model was used to simulate the dynamics of airway occlusion and reopening during assisted ventilation. It accounts for interactions between different airways, but not for the effect of gravity. In the current manuscript, we follow the approach of Halpern *et al.* (1998) for representing the tracheobronchial tree, but we use our augmented WRIBL model from Dietze *et al.* (2020), which accounts for inertia, gravity, axial viscous diffusion and full dynamic coupling between liquid and gas, to represent the liquid plugs.

In addition to work on low-dimensional modelling, many studies have been dedicated to the DNS of liquid plugs, i.e. based on the full Navier–Stokes equations. We provide a brief summary of such works next, whereby we focus on studies that have demonstrated the relevance of the additional effects included in our WRIBL model, and on liquid-plug features that have been identified as critical in airway occlusion, and thus need to be accurately predicted by any low-dimensional model. Fujioka & Grotberg (2004) simulated pressure-driven travelling-plug solutions (TPS), i.e. solutions that do not change in the reference frame of the plug, in a plane channel for liquids used in different medical settings, i.e. Survanta (for SRT) and Perflubron (for partial liquid ventilation). The authors observed the loss of TPS, constituting the occlusion/reopening limit, at large values of the capillary number,  $Ca$ , and they discovered the existence of a large vortex in the reference frame of the liquid plug. Further, it was shown that the tangential wall shear stress varies greatly along the axial dimension of the liquid film and that its maximum magnitude is attained at the precursory capillary ripple preceding the front of the liquid plug, which is visible in figure 1. Zheng, Fujioka & Grotberg (2007) later demonstrated for this configuration that inertia reduces the thickness of the trailing liquid film deposited by the liquid plug. Further, inertia was shown to increase the amplitude of the precursory capillary ripple, and, consequently, the maximum wall stresses. Ubal *et al.* (2008) constructed a stability diagram for pressure-driven TPS in a cylindrical tube for  $\Pi_\mu = \Pi_\rho = 0$ . In a transient setting, unstable TPS can be associated with plug rupture, i.e. airway reopening. The authors also confirmed the existence of a moving-frame vortex in the liquid plug for their cylindrical configuration.

Another group of works has focused on transient DNS of the liquid-plug dynamics. Fujioka, Takayama & Grotberg (2008) simulated pressure-driven liquid plugs in a cylindrical tube for  $\Pi_\mu = \Pi_\rho = 0$ , where the leading film thickness was imposed as a control parameter, which is representative of SRT conditions. Based on this, the authors determined how different control parameters affect the long-term fate of a liquid plug, i.e. whether the plug ruptures, attains a TPS or grows indefinitely. Further, the authors demonstrated via a dimensional analysis that inertial effects cannot necessarily be neglected in the case of airway closure, where the liquid viscosity is lower than for SRT. Finally, the authors confirmed that the precursory capillary ripple in front of the liquid plug develops the largest wall stresses and showed that the axial wall pressure derivative attains very large values there. Further, these different stress measures were shown to attain values sufficiently large to cause epithelial cell damage in the case of SRT, and to increase with increasing surface tension. Hassan *et al.* (2011) extended the work of Fujioka *et al.* (2008) by accounting for an active-gas phase and showed that this effect, as well as the effect of inertia, modifies the critical conditions for plug rupture. Olgac & Muradoglu (2013) performed similar simulations in order to mimic SRT in a subregion

of the tracheobronchial tree, i.e.  $7 \leq n \leq 19$ , and evaluated the associated maximum wall stresses. The authors concluded that the most dangerous conditions with respect to epithelial cell damage occur in the most distal airways (farthest from the trachea).

In the context of airway occlusion, Muradoglu *et al.* (2019) performed DNS of pressure-driven liquid plugs and studied the effect of a soluble surfactant. The authors showed that the surfactant reduces the maximum stress magnitudes associated with plug rupture, i.e. airway reopening, by approximately 20 %, whereas it delays plug rupture by approximately 10 %. Other authors performed DNS that account for the non-Newtonian rheology of mucus. For example, Hu, Romano & Grotberg (2020) showed that the presence of a yield stress delays plug rupture and Romano *et al.* (2021) showed that the visco-elastic rheology of mucus, which in the case of cystic fibrosis becomes dominated by the elastic response, can cause a second very significant wall stress peak after initial airway occlusion, thus increasing the danger of epithelial cell damage.

We turn now to experimental investigations of liquid plugs in narrow geometries, focussing again on works related to airway occlusion. Baudoin *et al.* (2013) modelled pulmonary airways via horizontal single-channel and branched microfluidic networks and studied airway reopening scenarios in trains of liquid plugs under an imposed pressure drop. The authors showed that the first plug rupture entrains and accelerates the next rupture events in the form of a cascade. Later, Hu *et al.* (2015) performed similar experiments with a viscoelastic test liquid, mimicking conditions in an  $n = 12$  airway. Camassa, Ogrosky & Olander (2014) and Camassa, Ogrosky & Olander (2017) performed seminal occlusion experiments that identified the threshold for liquid-plug formation in vertical cylindrical tubes. These experiments are particularly challenging to reproduce via low-dimensional models, as high-viscosity liquids were used, where axial viscous diffusion becomes relevant. In Dietze *et al.* (2020), we showed that accounting for this effect in our WRIBL model was necessary to capture the experimental occlusion threshold, which we predicted based on the loss of travelling-wave solutions (TWS). In the current manuscript, we will show that our augmented WRIBL model accurately captures the liquid plugs observed in these experiments.

Magniez *et al.* (2016) studied pressure-driven liquid plugs in an individual horizontal narrow cylindrical tube, mimicking airways with  $n \geq 9$ , at moderate values of  $Ca$ . The authors introduced a lubrication model similar to Fujioka *et al.* (2016) with which they identified TPS. Then, they showed experimentally that liquid plugs evolve towards plug rupture when their initial length is shorter than the TPS, whereas they keep accumulating liquid when their initial length is longer than the TPS. Mamba *et al.* (2018) used the same experimental set-up, this time focussing on plug rupture under cyclic forcing in the case of an initially dry tube wall. The authors found that cyclic gas flow rate variations lead to a periodic plug motion, whereas cyclic gas pressure variations lead to a cascading reduction of the plug volume and, eventually, plug rupture. The authors caution that their study is not fully representative of mucus plug dynamics under breathing conditions. Although their forcing frequency,  $f^* = 0.25$  Hz, was close to the typical breathing frequency,  $f^* = 0.33$  Hz, the viscosity of the employed liquid,  $\mu_1 = 5.1 \times 10^{-3}$  Pa s, was much smaller than the representative viscosity of mucus, i.e.  $\mu_1 = 13 \times 10^{-3}$  Pa s (Muradoglu *et al.* 2019). Later, similar experiments were performed in channels with square cross-section (Mamba, Zoueshtiagh & Baudoin 2019; Srinivasan, Rahatgaonkar & Khandekar 2021) or by using a visco-elasto-plastic liquid (Bahrani *et al.* 2022).

We conclude our review of experimental works by discussing a series of highly sophisticated experiments that have clearly established a link between liquid plugs and epithelial cell damage (Bilek *et al.* 2003; Kay *et al.* 2004; Huh *et al.* 2007; Tavana *et al.* 2010, 2011). In these experiments, which were initiated by Bilek *et al.* (2003), real

epithelial cell tissue was subjected to pressure-driven liquid plugs within micro-channels, and both the degree of cell damage, via two dyes that allow distinguishing between live and dead cells, and the associated maximum magnitudes of wall stresses and their spatial derivatives, were measured. It was concluded in Kay *et al.* (2004) that the maximum of the axial pressure derivative,  $\partial_{x^*} p_w^*$ , which occurs near the plug front, is responsible for the main cell damage, i.e. high cell damage was observed for  $\partial_{x^*} p_w^* \sim 0.6 \text{ Pa } \mu\text{m}^{-1}$ , and that the exposure time to critical stress conditions is not relevant. Interestingly, the maximum magnitude of the axial derivative of the tangential wall shear stress,  $\partial_{x^*} \tau_w^*$ , was an order of magnitude lower in these experiments. By contrast, both stress derivatives were of comparable magnitude in the lubrication model computations of Fujioka *et al.* (2016). In our current manuscript, we come to the same conclusion based on our WRIBL model computations, which we have validated with DNS. These results are supported by the work of Tavana *et al.* (2011), who performed DNS for conditions corresponding to their own cell damage experiments in a micro-channel, showing that  $\partial_{x^*} p_w^* \sim 0.6 \text{ Pa } \mu\text{m}^{-1}$  and  $\partial_{x^*} \tau_w^* \sim 0.6 \text{ Pa } \mu\text{m}^{-1}$  attain similar levels. The authors concluded that both quantities are linked to cell damage and showed that the level of cell damage can be greatly reduced by adding a surfactant. In Huh *et al.* (2007), the experiments of Kay *et al.* (2004) were extended by generating dynamic plug rupture events and it was shown that these events are linked to substantial epithelial cell damage.

In the current manuscript, we introduce a low-dimensional approach for predicting liquid plugs in the pulmonary airways, as well as the associated maximum wall stresses and their spatial derivatives. Our approach relies on the augmented WRIBL model of Dietze *et al.* (2020) for the representation of liquid plugs, which we apply to track solutions via numerical continuation across the entire conducting zone of the tracheobronchial tree. In particular, we will show that this model allows us to establish a direct continuation path from TWS to TPS. Earlier studies based on thin-film models could only capture TWS. Although this allows us to predict a conservative threshold for plug formation, i.e. based on the limit point (LP) of TWS (Camassa *et al.* 2014, 2016, 2017; Ding *et al.* 2019), the properties of TPS, in particular the wall stresses they generate, and their range of existence could not be captured. We refer to Dietze *et al.* (2020) for a thorough review of such works and mention here only works that have been published since, i.e. Camassa *et al.* (2021), who studied the stability of TWS, Ogrosky (2021a), who accounted for an additional liquid layer representing the PCL (periciliary liquid), which bathes the beating cilia responsible for mucus clearance in the conducting zone, and Ogrosky (2021b), who studied the effect of a surfactant.

Further, our augmented WRIBL model was developed up to order  $\epsilon^2$  in the long-wave parameter, which allows accounting for axial viscous diffusion. In Dietze *et al.* (2020), we showed that this is important for representing the dynamics of high-viscosity annular liquid films, and this was confirmed by Ogrosky (2021a). In the current manuscript, we will show that accounting for both inertia and axial viscous diffusion is necessary to accurately represent liquid plugs over a large liquid viscosity range, thus distinguishing our model from liquid-plug models based on the lubrication approximation.

In comparison with previous studies relying on the DNS of liquid plugs, our continuation approach distinguishes itself by enabling a low-cost high-fidelity prediction of how travelling-state solutions (TSS), i.e. TWS and TPS, evolve across the conducting zone of the tracheobronchial tree, as the airway generation,  $n$ , is increased. In particular, it allows us to predict critical conditions for airway occlusion and the occurrence of wall stresses with high potential for epithelial cell damage, as well as the effect of the relevant control parameters thereon. This may prove useful in the design of drugs and protocols for the treatment of pulmonary diseases. We use the approach of Halpern *et al.* (1998) to

represent the branching nature of the tracheobronchial tree, i.e. we assume that all airway properties evolve continuously with  $n$ , according to the lung architecture model of Weibel & Gomez (1962). Importantly, we track TSS that are most likely to emerge in a real system, by imposing the linearly most-amplified wavelength in our continuation calculations, which is obtained by simultaneously solving the linear stability problem. Thereby, we distinguish between convective instability (CI) and absolute instability (AI) regimes, which allows us to identify the critical airway generation for CI/AI transition. Also, our WRIBL calculations account for gravity and an active-gas phase, which were neglected in most of the above-discussed DNS studies. Gravity is not necessarily negligible, e.g. for airway generation  $n = 7$ , the Bond number,  $Bo = \rho_1 g R^{*2} / \sigma = 1.6$ , where  $g$  denotes the gravitational acceleration, and where we have taken  $\rho_1 = 1000 \text{ kg m}^{-3}$  for the mucus density and  $\sigma = 0.02 \text{ N m}^{-1}$  for the surface tension of mucus, according to Muradoglu *et al.* (2019). And, in the presence of surfactant, this value further increases (Muradoglu *et al.* 2019).

Our manuscript is structured as follows. In §2, we will introduce the employed augmented WRIBL model, followed by §3, where we will describe the numerical approaches used to solve the model equations, i.e. linear stability analysis, numerical continuation of nonlinear TSS and transient computations of liquid-plug formation in periodic or open domains. In §4, we will demonstrate the predictive power of the augmented WRIBL model in terms of representing liquid plugs, by comparing with experiments and DNS. In §5, we will present our results. There, we will use numerical continuation of TSS to predict the effect of different parameters, i.e. airway generation,  $n$ , airway orientation vs gravity, mucus properties, air flow rate and airway radius, on the threshold for airway occlusion (§5.1) and on the maximum wall stresses and spatial wall stress derivatives (§5.2). Conclusions will be drawn in §6.

## 2. Mathematical description

We consider the flow sketched in figure 1(a), a liquid film (subscript,  $k = 1$ ) lining the inner surface of a narrow cylindrical tube of radius,  $R^*$  (the star symbol denotes dimensional quantities throughout) in contact with a gas phase in the core (subscript,  $k = 2$ ). Both fluids are considered Newtonian with constant fluid properties and the flow as laminar. As a result of the Plateau–Rayleigh instability, the liquid can come to occlude the tube in the form of travelling plugs that enclose a gas bubble in between. Figure 1(b) represents streamlines within such a flow for a gravity-driven vertical configuration.

We denote as  $d$  the core radius, i.e. the radial distance between the tube axis and the liquid–gas interface, and as  $h$  the liquid film thickness. We describe the flow in the framework of the long-wave approximation, which implies  $\varepsilon = R^* / \Lambda^* \ll 1$ , introducing the long-wave parameter  $\varepsilon$  and the wavelength,  $\Lambda^*$ , of the plug/bubble arrangement. Based on the most-amplified wavelength of the classical Plateau–Rayleigh instability,  $\Lambda^* = 2\sqrt{2}\pi d_0^*$ , where the subscript zero denotes the primary flow, we obtain  $\varepsilon = (R^* / d_0^*) / (2\sqrt{2}\pi)$ . As we will see, liquid-plug formation occurs for  $d_0^* / R^* \sim 0.8$  in our study, yielding  $\varepsilon \sim 10^{-1}$ .

The studied flow is governed by the phase-specific (subscript  $k$ ) Navier–Stokes and continuity equations truncated at  $\mathcal{O}(\varepsilon^2)$ , and written here in non-dimensional form

$$X_k \varepsilon \partial_t u_k + \varepsilon u_k \partial_x u_k + \varepsilon v_k \partial_r u_k = -\varepsilon \partial_x p_k + \frac{1}{Re_k} \left\{ \varepsilon^2 \partial_{xx} u_k + \frac{1}{r} \partial_r (r \partial_r u_k) \right\} + \frac{X_k^2}{Fr^2}, \quad (2.1a)$$

$$0 = -\varepsilon \partial_r p_k + \varepsilon^2 \frac{1}{Re_k} \partial_r \left\{ \frac{1}{r} \partial_r (rv_k) \right\}, \tag{2.1b}$$

$$\partial_x u_k + \frac{1}{r} \partial_r (rv_k) = 0, \tag{2.1c}$$

where  $x$  and  $r$  denote the axial and radial coordinates,  $u_k$ ,  $v_k$  and  $p_k$  the corresponding velocity components and pressure in phase  $k$  and  $t$  denotes time. Also, we have  $X_1 = 1$  and  $X_2 = \Pi_u^{-1}$ , and  $\Pi_u = \mathcal{U}_2/\mathcal{U}_1$  denotes the velocity scale ratio,  $Re_k = \mathcal{U}_k \mathcal{L}/\nu_k$  denotes the phase-specific Reynolds number and  $Fr = \mathcal{U}_1/\sqrt{g\mathcal{L}}$  denotes the Froude number. Here, we have applied the following scaling:

$$u_k = \frac{u_k^*}{\mathcal{U}_k}, \quad v_k = \frac{v_k^*}{\varepsilon \mathcal{U}_k}, \quad x = \varepsilon \frac{x^*}{\mathcal{L}}, \quad r = \frac{r^*}{\mathcal{L}}, \quad t = \varepsilon t^* \frac{\mathcal{U}_1}{\mathcal{L}}, \quad p_k = \frac{p_k^*}{\rho_k \mathcal{U}_k^2}, \tag{2.2a-f}$$

choosing the tube radius as the length scale,  $\mathcal{L} = R^*$ , and the phase-specific superficial velocities,  $\mathcal{U}_k = \bar{q}_k^*/\pi/R^{*2}$ , as the velocity scales, where  $\bar{q}_k^*$  denotes the phase-specific average cross-sectional flow rate. The truncated inter-phase coupling conditions for the normal and tangential stresses at  $r = d$  are

$$\varepsilon p_1 + \varepsilon We \varepsilon^2 \kappa - \frac{2\varepsilon^2}{Re_1} \partial_r v_1 = \Pi_\rho \Pi_u^2 \varepsilon p_2 - \Pi_\mu \Pi_u \frac{2\varepsilon^2}{Re_1} \partial_r v_2, \tag{2.3a}$$

$$\begin{aligned} & -(\partial_r u_1 + \varepsilon^2 \partial_x v_1) + 2\varepsilon^2 \partial_x d (\partial_x u_1 - \partial_r v_1) \\ & = \Pi_u \Pi_\mu \{ -(\partial_r u_2 + \varepsilon^2 \partial_x v_2) + 2\varepsilon^2 \partial_x d (\partial_x u_2 - \partial_r v_2) \}, \end{aligned} \tag{2.3b}$$

where  $\Pi_\mu = \mu_2/\mu_1$  and  $\Pi_\rho = \rho_2/\rho_1$  denote the viscosity and density ratios,  $We = \sigma/\rho_1/\mathcal{U}_1^2/\mathcal{L}$  the Weber number and  $\kappa$  the (truncated) surface curvature

$$\kappa = \frac{1}{d} - \frac{1}{2} \frac{\partial_x d^2}{d} - \partial_{xx} d = \kappa_\varphi - \partial_{xx} d. \tag{2.4}$$

We will also use the Kapitza number,  $Ka = \sigma/(\rho_1 g^{1/3} \nu_1^{4/3})$ , to characterize the working liquid. Further, we have the kinematic coupling conditions at  $r = d$

$$u_1 = \Pi_u u_2, \tag{2.5a}$$

$$v_1 = \Pi_u v_2, \tag{2.5b}$$

$$X_k^{-1} v_k = \frac{dd}{dt} = \partial_t d + X_k^{-1} u_k \partial_x d, \tag{2.5c}$$

and the radial boundary conditions

$$u_1|_{r=R} = 0, \quad \partial_r u_2|_{r=0} = 0, \tag{2.6a}$$

$$v_1|_{r=R} = 0, \quad v_2|_{r=0} = 0. \tag{2.6b}$$



*Liquid plugs in narrow tubes*

We simplify the truncated governing equations further by applying the WRIBL technique (Kalliadasis *et al.* 2012). We only sketch the procedure here, referring the reader to Dietze *et al.* (2020) for details. First, we substitute  $p_k$  in (2.1a) via an integration of (2.1b), yielding the phase-specific boundary-layer equations, BLE<sub>k</sub>

$$\begin{aligned} \text{BLE}_k : \quad & X_k \varepsilon \partial_r u_k + \varepsilon u_k \partial_x u_k + \varepsilon v_k \partial_r u_k = -\varepsilon \partial_x [p_k|_d] + \frac{X_k^2}{Fr^2} \\ & -\varepsilon^2 \frac{1}{Re_k} \partial_x [\partial_x u_k|_d] + \frac{1}{Re_k} \{2 \varepsilon^2 \partial_{xx} u_k + \partial_{rr} u_k\}. \end{aligned} \quad (2.7)$$

Next, we decompose the velocity components according to

$$u_k(x, r, t) = \underbrace{\hat{u}_k(x, r, t)}_{\mathcal{O}(\varepsilon^0)} + \underbrace{u_k^{(1)}(x, r, t)}_{\mathcal{O}(\varepsilon^1)}, \quad (2.8a)$$

$$v_k(x, r, t) = \underbrace{\hat{v}_k(x, r, t)}_{\mathcal{O}(\varepsilon^0)} + \underbrace{v_k^{(1)}(x, r, t)}_{\mathcal{O}(\varepsilon^1)}, \quad (2.8b)$$

introducing the leading-order velocity  $\hat{u}_k$ , which is governed by

$$\frac{1}{r} \partial_r (r \partial_r \hat{u}_k) = Z_k, \quad (2.9a)$$

$$\partial_r u_1|_d = \Pi_\mu \Pi_u \partial_r u_2|_d, \quad u_1|_d = \Pi_u u_2|_d, \quad u_1|_R = \partial_r u_2|_0 = 0, \quad (2.9b)$$

$$2\pi \int_{d(x,t)}^R r \hat{u}_1 dr = q_1(x, t), \quad 2\pi \int_0^{d(x,t)} r \hat{u}_2 dy = q_2(x, t), \quad (2.9c)$$

where  $q_k$  denotes the phase-specific cross-sectional flow rate. This leads to

$$\hat{u}_k = f_{ki}(r, d) q_i(x, t), \quad (2.10a)$$

$$\hat{v}_1 = -\frac{1}{r} \int_r^1 \tilde{r} \partial_x \hat{u}_1 d\tilde{r}, \quad \hat{v}_2 = \frac{1}{r} \int_0^r \tilde{r} \partial_x \hat{u}_2 d\tilde{r}, \quad (2.10b)$$

where  $\hat{v}_k$  is obtained via integration of (2.1c). Then, we introduce (2.8) in the BLE<sub>k</sub> from (2.7), and combine the resulting equations via a weighted integration

$$\int_{d(x,t)}^R r w_1(r) \text{BLE}_1 dr + \Pi_\rho \Pi_u^3 \int_0^{d(x,t)} r w_2(r) \text{BLE}_2 dr, \quad (2.11)$$

where the weight functions,  $w_k$ , satisfy

$$w_k(r, d) = f_{k1}(r, d) - \Pi_u^{-1} f_{k2}(r, d). \quad (2.12)$$

Finally, truncating (2.11) at  $\mathcal{O}(\varepsilon^2)$ , dropping inertial corrections of order  $\mathcal{O}(Re_k \varepsilon u_k^{(1)})$  and introducing the source term  $\Pi_\varphi$ , yields the final integral momentum equation rescaled by

setting  $\varepsilon = 1$

$$S_i \partial_t q_i + F_{ij} q_i \partial_x q_j + G_{ij} q_i q_j \partial_x h = \frac{We}{2\pi} \partial_x \kappa + \Pi_\varphi + \frac{1}{2\pi} Fr^{-2} (1 - \Pi_\rho) + \frac{1}{2\pi} C_i q_i + J_i q_i \partial_x h^2 + K_i \partial_x q_i \partial_x h + L_i q_i \partial_{xx} h + M_i \partial_{xx} q_i, \tag{2.13a}$$

to which are added the integral continuity equations

$$\partial_t d - \frac{1}{2\pi d} \partial_x q_1 = 0, \quad \partial_t d + \frac{\Pi_u}{2\pi d} \partial_x q_2 = 0, \tag{2.13b}$$

obtained through integration of (2.1c), with the help of (2.5c). The model coefficients  $S_i$ ,  $F_{ij}$ ,  $G_{ij}$ ,  $C_i$ ,  $J_i$ ,  $K_i$ ,  $L_i$  and  $M_i$  are known functions of  $d$  (Dietze 2022). Equations (2.13a) and (2.13b) constitute the 3-equation WRIBL model of Dietze *et al.* (2020) for the three unknowns,  $d$ ,  $q_1$  and  $q_2$ .

The source term,  $\Pi_\varphi$ , is designed to represent liquid pseudo-plugs

$$\Pi_\varphi = -\frac{We}{2\pi} \Pi_{CRL} \exp \left[ \lambda \left( 1 - \frac{d(x, t)}{d_{plug}} \right) \right] \partial_x \kappa_\varphi, \tag{2.13c}$$

where  $\Pi_{CRL}$  sets the magnitude of  $\Pi_\varphi$ ,  $\lambda$  is a slope coefficient ( $\lambda = 1$  in all our computations) and  $d_{plug}$  designates the core radius of a pseudo-plug. By pseudo-plug, we mean a liquid annulus that fills the entire tube cross-section except for an arbitrarily thin filament of core fluid with  $d = d_{plug} \ll 1$  ( $d_{plug} = 0.01$  in our computations). Thanks to this approach, liquid plugs can be represented without violating the mathematical requirement of a finite core radius  $d(x)$ .

The source term,  $\Pi_\varphi$ , is comparable to the so-called disjoining pressure typically used for imposing a precursor film in lubrication models for contact line problems (Thiele *et al.* 2001). At  $d = d_{plug}$  and  $\Pi_{CRL} = 1$ ,  $\Pi_\varphi$  exactly cancels the azimuthal capillary term,  $(We/2\pi) \partial_x \kappa_\varphi$ , in (2.13a), which is responsible for the Plateau–Rayleigh instability, thus rendering the cylindrical surface of the pseudo-plug stable. For  $d > d_{plug}$ ,  $\Pi_\varphi < (We/2\pi) \partial_x \kappa_\varphi$  and the Plateau–Rayleigh mechanism remains dominant, whereas the opposite holds for  $d < d_{plug}$ . As a result, the film surface is attracted toward  $d = d_{plug}$  from both sides. Because  $\Pi_\varphi$  varies very sharply around  $d_{plug}$ , this effect is felt only when  $d$  is close to  $d_{plug}$ , and it translates into a very strong repulsion of the film surface in the limit  $d \rightarrow 0$ . Moreover, the cylindrical surface  $d = d_{plug}$  can be rendered entirely stable in the presence of a mean flow via an appropriate choice of  $\Pi_{CRL} \geq 1$  (see § 3.1).

At the LPs of a real liquid plug,  $d \rightarrow 0$  and  $\partial_x d \rightarrow \pm \infty$ . Of course, such an infinitely steep liquid–gas interface cannot be represented in the framework of the long-wave approximation. Consequently, the leading and trailing fronts of pseudo-plugs computed with our augmented WRIBL model (2.13a) are less steep than for real plugs. We will show in § 4 that this does not prevent our model from producing excellent estimates of different plug measures (see e.g. figure 5). Nonetheless, a static approximation (Lamstaes & Eggers 2017) can improve our prediction of the plug shape. Here, following Bretherton (1961), we approximate the liquid–gas interface by a spherical cap (see e.g. figure 6), denoted by the subscript  $sc$ , in regions where the interface slope,  $\partial_x d$ , is too large for the long-wave approximation to hold, i.e. for  $|\partial_x d| \geq \epsilon^{max}$ , whereby we choose  $\epsilon^{max} \sim 1$ . The radius,  $R_{sc}$ , and centre,  $x_{sc}$ , of the spherical cap are obtained by requiring continuity of  $d$  and  $\partial_x d$

across the patching point,  $(x_p, d_p)$

$$d_p = d|_{x=x_p} \equiv \left\{ R_{sc}^2 - (x_p - x_{sc})^2 \right\}^{1/2}, \quad (2.14)$$

$$\partial_x d|_{x=x_p} = \epsilon^{max} \equiv -\frac{x_p - x_{sc}}{d_p}. \quad (2.15)$$

We point out that a spherical approximation is valid only when the effect of gravity is weak over the axial length scale of the cap and liquid viscous stresses are dominated by surface tension (small capillary number,  $Ca$ ), which turns out to be the case for typical conditions of liquid plug formation in the pulmonary airways (see figures 13*d* and 15*c*).

Our WRIBL model can be extended with a fourth evolution equation for the gas pressure at the liquid–gas interface,  $p_2|_d$ . This is obtained by performing the operation in (2.11) with the modified weight functions,  $\tilde{w}_k = f_{k1}(r, d) + \Pi_u^{-1} f_{k2}(r, d)$ , in which case  $p_2|_d$  does not cancel from (2.7) and can be solved for, yielding

$$\begin{aligned} 2\Pi_\rho \Pi_u^2 \partial_x [p_2|_d] &= -\tilde{S}_i \partial_t q_i + \text{NLP}(x, t), \\ \text{NLP}(x, t) &= -\tilde{F}_{ij} q_i \partial_x q_j - \tilde{G}_{ij} q_i q_j \partial_x h \\ &\quad + \frac{We}{2\pi} \partial_x \kappa + \frac{1}{2\pi} Fr^{-2} (1 + \Pi_\rho) + \frac{1}{2\pi} \tilde{C}_i q_i \\ &\quad + \tilde{J}_i q_i \partial_x h^2 + \tilde{K}_i \partial_x q_i \partial_x h + \tilde{L}_i q_i \partial_{xx} d + \tilde{M}_i \partial_{xx} q_i, \end{aligned} \quad (2.16)$$

where the tilde distinguishes coefficients from their counterparts in the momentum equation (2.13*a*). Introducing the total flow rate,  $q_{tot} = q_1 + \Pi_u q_2$ , this pressure equation (2.16) can be integrated across the domain length  $L$  (Einstein’s summation convention is applied below)

$$\begin{aligned} \Delta p_2 &= \int_0^L \partial_x [p_2|_h] dx = \frac{1}{2\Pi_\rho \Pi_u^2} \left\{ \int_0^L \text{NLP}(x, t) dx - \int_0^L \tilde{S}_i \partial_t q_i dx \right\} \\ &= \frac{1}{2\Pi_\rho \Pi_u^2} \left\{ \int_0^L \text{NLP}(x, t) dx - \int_0^L \left( \tilde{S}_1 - \frac{\tilde{S}_2}{\Pi_u} \right) \partial_t q_1 dx - \partial_t q_{tot} \int_0^L \frac{\tilde{S}_2}{\Pi_u} dx \right\}, \end{aligned} \quad (2.17)$$

and then used as an integral condition on the pressure drop  $\Delta p_2$ , or, when  $q_2$  is imposed, to evaluate  $\Delta p_2$  *a posteriori*. For this, we introduce the normalized pressure gradient  $M$

$$M = \frac{\Delta p_2}{\rho_2 g L}. \quad (2.18)$$

In (2.13*a*), the velocity corrections,  $u_k^{(1)}$ , were eliminated via truncation and an appropriate choice of the weight functions,  $w_k$  (2.12). However, they can be reconstructed *a posteriori*, after having obtained a solution for  $d$  and  $q_k$ . For this, we insert (2.8) and (2.10*a*) into (2.1*a*), (2.1*b*), (2.3*b*), (2.5*a*) and (2.6*a*), eliminate  $p_k$  via cross-differentiation, truncate at  $\mathcal{O}(\epsilon^2)$  and drop terms of  $\mathcal{O}(Re_k \epsilon u_k^{(1)})$ . The resulting boundary value problem

can be readily solved for  $u_k^{(1)}$

$$u_1^{(1)} = C_1 r^6 + C_2 r^4 + C_3 r^2 + C_4 + \ln(r)^2 \{C_5 r^2 + C_6\} + \ln(r) \{C_7 r^4 + C_8 r^2 + C_9\}, \tag{2.19a}$$

$$u_2^{(1)} = D_1 r^6 + D_2 r^4 + D_3 r^2 + D_4, \tag{2.19b}$$

where the coefficients,  $C_i$  and  $D_i$ , are known functions of  $d$ ,  $q_k$  and their derivatives. The cross-stream velocity corrections  $v_k^{(1)}$  are again obtained via integration of (2.1c), using (2.8), (2.10a) and (2.19). The velocity corrections  $u_k^{(1)}$  and  $v_k^{(1)}$  will be useful for producing accurate predictions of the wall stresses and their spatial derivatives in §§ 4 and 5.2.

### 3. Numerical methods

We perform three types of numerical computations based on our WRIBL model (2.13). Linear stability calculations, which allow us to identify the most-dangerous surface structures (waves or liquid plugs) emanating from interfacial instability. Numerical continuation of TSS with the continuation software Auto07P (Doedel 2008) allows us to identify the threshold at which nonlinear TWS transform into TPS. And, thirdly, spatio-temporal computations using custom codes based on a finite-difference spatial discretization. In the latter case, we distinguish computations with periodicity boundary conditions on a domain spanning one wavelength,  $\Lambda$ , from computations on an open domain with inlet/outlet conditions.

#### 3.1. Linear stability analysis

We consider the primary flow of an annular liquid film of core radius,  $d_0$ , and flow rate,  $q_{10}$ , in contact with a gas of flow rate,  $q_{20}$ , and perturb it in terms of  $d$  and  $q_k$

$$d = d_0 + d' = d_0 + \hat{d} \exp \{i(kx - \omega t)\}, \tag{3.1a}$$

$$q_k = q_{k0} + q'_k = q_{k0} + \hat{q}_k \exp \{i(kx - \omega t)\}, \tag{3.1b}$$

where  $i = \sqrt{-1}$ , and where we have assumed the infinitesimal perturbations,  $d'$  and  $q'_k$ , grow according to exponential modes with wavenumber,  $k$ , and angular frequency,  $\omega$ . Their amplitudes,  $\hat{d}$  and  $\hat{q}_k$ , are linked via the continuity equations (2.13b)

$$\hat{q}_1 = -2\pi d_0 \hat{d} \frac{\omega}{k}, \quad \hat{q}_2 = 2\pi d_0 \Pi_u^{-1} \hat{d} \frac{\omega}{k}. \tag{3.2a,b}$$

Inserting (3.1) into (2.13a), and linearizing around the primary flow, we obtain the dispersion relation

$$\begin{aligned} \text{DR} &= i \omega^2 2\pi d \{ \Pi_u^{-1} S_2 - S_1 \} \\ &+ i k \omega 2\pi d \{ -\Pi_u^{-1} F_{22} q_2 + F_{21} q_2 - \Pi_u^{-1} F_{12} q_1 + F_{11} q_1 \} \\ &+ i k^2 \{ G_{22} q_2^2 + 2 G_{12} q_2 q_1 + G_{11} q_1^2 \} \end{aligned}$$

$$\begin{aligned}
 & - \left\{ \omega C_1 d + k \frac{1}{2\pi} \partial_d C_1 q_1 \right\} + \left\{ \omega \Pi_u^{-1} C_2 d - k \frac{1}{2\pi} \partial_d C_2 q_2 \right\} \\
 & - i^2 k^3 \{L_1 q_1 + L_2 q_2\} + i^2 k^2 \omega 2\pi d \{ \Pi_u^{-1} M_2 - M_1 \} \\
 & - i^3 k^4 We \frac{1}{2\pi} - i k^2 We \frac{1}{2\pi} \frac{1}{d^2} \left\{ 1 - \Pi_{CRL} \exp \left[ \lambda \left( 1 - \frac{d}{d_{plug}} \right) \right] \right\} = 0, \quad (3.3)
 \end{aligned}$$

where we have dropped the subscript 0 for convenience.

The capillary term involving  $i k^2 We$  is due to the azimuthal curvature of the film surface, and it includes the source term,  $\Pi_\phi$ , introduced in (2.13c). Through  $\Pi_{CRL}$ , this term can be tuned to fully stabilize a cylindrical surface at  $d = d_{plug} \ll 1$ .

In the classical Plateau–Rayleigh configuration, where  $q_k = \Pi_\mu = \Pi_\rho = 0$ , assuming temporally growing modes, i.e.  $k, \omega_i \in \mathbb{R}$  and  $\omega = i\omega_i \in \mathbb{C}$ , the cutoff wavenumber,  $k_c$ , is given by

$$k_c = \frac{1}{d} \left\{ 1 - \Pi_{CRL} \exp \left[ \lambda \left( 1 - \frac{d}{d_{plug}} \right) \right] \right\}^{1/2}. \quad (3.4)$$

In the limit  $\Pi_{CRL} = 0$ , our model recovers the analytical cutoff wavenumber  $k_c = 1/d$  for all core radii,  $d$ . By contrast, when setting  $\Pi_{CRL} = 1$ , full stabilization ( $k_c = 0$ ) is achieved for  $d/d_{plug} = 1$ , without affecting stability for  $d/d_{plug} \ll 1$ . This makes it possible to produce nonlinear pseudo-plug solutions with our WRIBL model, where the plug is represented via a liquid annulus filling almost the entire tube cross-section, except for a narrow cylindrical gas filament of radius  $d \sim d_{plug}$  around the tube axis, which is stable and does not pinch.

Conditions for obtaining stable pseudo-plugs may change when there is a sufficiently strong primary flow, in which case the stability limit may be affected by inertia, in contrast to the classical Plateau–Rayleigh configuration discussed above. We discuss this based on figure 2, which represents stability calculations for spatially growing modes, i.e.  $k = k_r + ik_i \in \mathbb{C}$  and  $\omega \in \mathbb{R}$ . Figure 2(a) compares dispersion curves of the spatial growth rate,  $-k_i$ , obtained from (3.3) with the solution of the full Orr–Sommerfeld eigenvalue problem (Hickox 1971), for three examples of stratified gravity-driven liquid films within a cylindrical tube. For all three working liquids, which correspond to different experiments (Dao & Balakotaiah 2000; Piroird *et al.* 2011; Camassa *et al.* 2014) and cover a wide  $Ka$  range, our model predictions are in good agreement with the Orr–Sommerfeld solution.

For the low-viscosity silicone oil (blue open circles), the cutoff wavenumber  $k_c d_0$  is shifted with respect to the classical Plateau–Rayleigh solution,  $k_c d_0 = 1$ , as a result of the inertia-driven Kapitza instability. Thus, in the passive-core limit ( $\Pi_\mu = \Pi_\rho = 0$ ),  $\Pi_{CRL} > 1$  is required to fully stabilize a pseudo-plug at  $d = d_{plug}$ . We show this in figure 2(b), which represents  $-k_i(\omega)$  curves for a pseudo-plug of  $d = d_{plug} = 0.01$ . Comparing the dashed and dot-dashed curves, we see that full stabilization is achieved by changing  $\Pi_{CRL}$  from 1 to 1.01. In the case of an active-core fluid, e.g. air, full stabilization is already achieved at  $\Pi_{CRL} = 1$  (solid curve), but the growth rate is only very slightly negative in this case ( $-k_i$  has been multiplied by  $10^3$  in the graph).

Above, we have used linear stability analysis to demonstrate that stable pseudo-plug solutions can be obtained with our WRIBL model (2.13). In addition, we will use linear stability calculations to identify the most-dangerous linear instability modes, i.e. those that are most likely to emerge in a real system, and thus select the nonlinear solutions that will be of interest in the next section. In such calculations, we will distinguish between CI and AI modes. We will discuss this in detail in § 3.2.

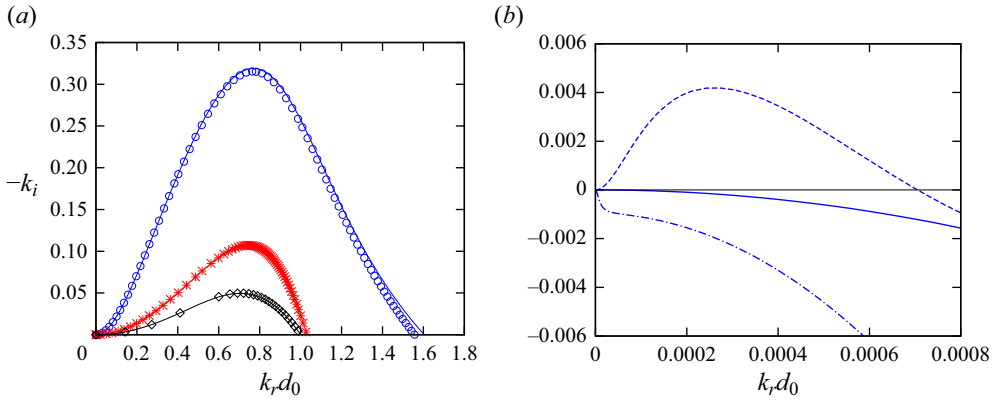


Figure 2. Spatial linear stability of an annular liquid film in contact with air. Symbols: WRIBL; solid lines: Orr–Sommerfeld. (a) Falling liquid film. Circles:  $R^* = 1.5$  mm,  $Ka = 121.4$  (silicone oil II/air I in table 1),  $Re_1 = 15.4$ ,  $M = 1$ ; asterisks: run 13 in Dao & Balakotaiah (2000),  $R^* = 3.175$  mm,  $Ka = 3.5$  (glycerol(89%)-water/air I),  $Re_1 = 0.258$ ,  $M = 1$ , diamonds: experiment from figure 3(c) of Camassa *et al.* (2014),  $Ka = 3.3 \times 10^{-3}$  (silicone oil I, air I in table 1),  $R^* = 5$  mm,  $Re_1 = 4.5 \times 10^{-4}$ ,  $M = 1$ ; (b) stability of a pseudo-plug obtained with our augmented WRIBL model (2.13c). Silicone oil film from panel (a):  $d_0 = d_{plug} = 0.01$ ,  $\lambda = 1$ . Dashed:  $\Pi_{CRL} = 1$ ,  $\Pi_\mu = \Pi_\rho = 0$ ; dot-dashed:  $\Pi_{CRL} = 1.01$ ,  $\Pi_\mu = \Pi_\rho = 0$ ; solid:  $\Pi_{CRL} = 1$  ( $-k_i$  has been multiplied by  $10^3$ ).

### 3.2. Travelling-state solutions

To construct TSS, we introduce the wave/plug celerity,  $c$ , and express the space and time derivatives in (2.13b) and (2.13a) via the wave coordinate  $\xi$

$$\xi = x - ct, \quad \partial_x = \partial_\xi, \quad \partial_t = -c \partial_\xi, \tag{3.5a-c}$$

thus transforming our system of partial differential equations into a dynamical system given by

$$d''' = NL(d, d', d'', q_1^{MF}, q_{tot}), \tag{3.6a}$$

$$q_1^{MF} = q_1 - \pi(R^2 - d^2)c = \bar{q}_1 - \pi(R^2 - \bar{d}^2)c, \tag{3.6b}$$

$$q_{tot} = q_1 + \Pi_u q_2 = \bar{q}_1 + \Pi_u \bar{q}_2, \tag{3.6c}$$

where primes denote differentiation with respect to  $\xi$ , bars signify averaging over the wavelength  $\Lambda$  in terms of  $\xi$ , the superscript MF refers to the wave-fixed moving reference frame and where we have used (3.6b) and (3.6c) to replace derivatives  $q_k^{(j)}$  by derivatives  $d^{(j)}$  in (3.6a). Equations (3.6b) and (3.6c) were obtained from the phase-specific continuity equations in (2.13b). Further,  $\bar{q}_k = \pi$  for the scaling used here.

The system is closed through the periodicity boundary conditions

$$d^{(j)}|_{\xi=0} = d^{(j)}|_{\xi=\Lambda}, \quad j = 0, 1, 2, \tag{3.6d}$$

and it is solved for fixed values of  $\bar{q}_1^*$  (controlled via  $Re_1$ ), which is enforced through the integral condition

$$\Lambda^{-1} \int_0^\Lambda q_1 d\xi = \bar{q}_1, \tag{3.7}$$

## Liquid plugs in narrow tubes

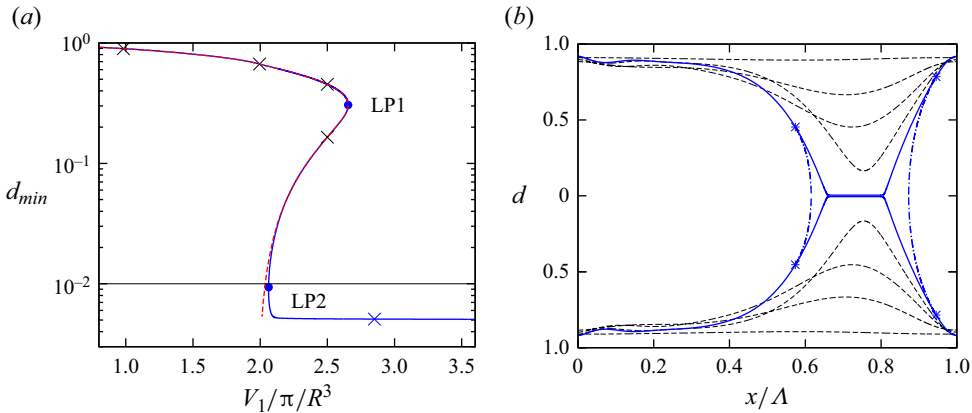


Figure 3. Transition from TWS to TPS. The TSS are based on our augmented WRIBL model (2.13a). Annular liquid film in contact with air within a vertical cylindrical tube:  $Ka = 121.4$  (silicone oil II and air I in table 1),  $R^* = 1.5$  mm,  $M = 1$ ,  $\Lambda = 5.4$ . (a) Minimal core radius,  $d_{min}$ , in terms of the normalized liquid volume. Solid blue:  $\Pi_{CRL} = \lambda = 1$ ,  $d_{plug} = 0.01$ ; dashed red:  $\Pi_{CRL} = 0$ ; profiles of TSS corresponding to crosses in panel (a). Toward the tube axis:  $V_1/\pi/R^3 = 1, 2, 2.5, 2.5, 2.85$ . Dot-dashed blue lines correspond to spherical-cap reconstruction (2.14) between the patching points (blue asterisks), where  $|\partial_x d| = \epsilon^{max} = 0.75$ .

and  $q_{tot}^*$  (via  $Re_2$ ), which is imposed either explicitly, or indirectly through an integral condition on the pressure drop (2.17)

$$\Delta p_2 2\Pi_\rho \Pi_u^2 = \int_0^\Lambda \text{NLP}(d, d', d'', d''', q_1^{\text{MF}}, q_{tot}) d\xi - \int_0^\Lambda (\tilde{S}_1 - \Pi_u^{-1} \tilde{S}_2) d'c d\xi. \quad (3.8)$$

The equation system given by (3.6) and (3.7), or by (3.6) and (3.8), is solved via numerical continuation using Auto07P (Doedel 2008). Figure 3 represents TSS obtained this way for the silicone oil and tube radius,  $R^* = 1.5$  mm, used in the experiments of Piroird *et al.* (2011), only that the cylindrical tube is oriented vertically here and that we have air and not water as the core phase. The dashed red line in figure 3(a), where we have plotted the minimal core radius,  $d_{min}$ , of TSS vs the liquid volume,  $V_1$ , corresponds to the standard model, i.e.  $\Pi_{CRL} = 0$ . The LP of this curve (LP1) corresponds to the occlusion bound identified in Dietze *et al.* (2020). Its upper branch corresponds to stable TWS and its lower branch to unstable TWS, as has been demonstrated by the stability calculations of Camassa *et al.* (2021). Thus, even though there is multiplicity of TWS for a fixed  $V_1$ , only TWS on the upper branch should prevail in an experiment. The lower TWS branch stops abruptly as the core radius tends to zero ( $d_{min} \rightarrow 0$ ). By contrast, the solid blue curve, which corresponds to our augmented model ( $\Pi_{CRL} = 1$ ,  $d_{plug} = 0.01$ ), displays a second LP (LP2), from which a branch of TPS originates. Figure 3(b) represents selected profiles (corresponding to crosses in figure 3a) of the liquid–gas interface along this curve, illustrating the evolution from TWS (dashed curves) to a TPS (solid blue curve). The dot-dashed blue curves correspond to the spherical-cap approximation (2.14), using  $\epsilon^{max} = 0.75$ , which allows us to represent more accurately the leading and trailing fronts of the liquid plug. We will use this approximation from here on to reconstruct these portions of TPS, i.e. starting from the patching points marked by asterisks in figure 3(b).

In our numerical continuation of TSS, we can impose the linearly most-dangerous wavenumber,  $k = 2\pi/\Lambda = k_{max}$ , which is obtained by simultaneously solving the dispersion relation (3.3) governing the linear response of the liquid film. Depending on the flow conditions, we distinguish between CI and AI modes. In the case of CI, we

choose a spatial stability formulation,  $\omega \in \mathbb{R}$ ,  $k \in \mathbb{C}$ , and  $k_{max}$  corresponds to the spatially most-amplified wavenumber

$$DR(\omega, k_{max}) = 0, \quad \partial_{\omega} k_i|_{k=k_{max}} = 0, \tag{3.9a}$$

where the expression for  $\partial_{\omega} k_i$  is obtained by rearranging  $\partial_{\omega} DR = 0$ . In the case of AI, we choose a spatio-temporal stability formulation (Brevdo *et al.* 1999),  $\omega \in \mathbb{C}$ ,  $k \in \mathbb{C}$ , and  $k_{max}$  corresponds to the absolute wavenumber

$$DR(\omega, k_{max}) = 0, \quad \frac{d}{dk} DR(\omega, k)|_{k=k_{max}} = 0, \quad \left. \frac{d\omega}{dk} \right|_{k=k_{max}} = 0, \tag{3.9b}$$

where  $d\omega/dk \in \mathbb{C}$  denotes the group velocity in the wall-fixed reference frame. For most of our calculations in § 5, a CI/AI transition is observed on a given TSS branch (marked by crosses, e.g. in figure 10). The transition point can be readily identified by detecting  $\omega_i = d\omega/dk = 0$ .

The primary flow underlying the solution of (3.9a) and (3.9b) is set according to the properties of the corresponding nonlinear TSS, i.e.  $d_0 = d_{VE}$  and  $q_{20} = \bar{q}_2$  or  $M_0 = M$ , depending on whether the gas flow rate (figure 10) or the gas pressure drop (figure 11) is imposed. Here,  $d_{VE}$  is the volume-equivalent core radius

$$d_{VE} = \left\{ 1 - \frac{1}{A} \int_0^A (1 - d^2) dx \right\}^{1/2}. \tag{3.10}$$

### 3.3. Transient periodic computations

We perform transient periodic computations to represent the dynamics of liquid-plug formation from an initially uniform liquid film. For this, our model equations (2.13a) and (2.13b) are solved by numerically advancing the solution in time, i.e. from  $t = t_{old}$  to  $t = t_{new}$ . Our equations are recast by eliminating  $q_2$  via (3.6c)

$$\partial_t q_1 + S_2 (\Pi_u S_1 - S_2)^{-1} \partial_t q_{tot} = NL(\partial_x d, \partial_x q_1) + \Pi_{\varphi} (\Pi_u S_1 - S_2)^{-1}, \tag{3.11a}$$

$$\partial_t d = \frac{1}{2\pi d} \partial_x q_1, \tag{3.11b}$$

and then integrated over the time increment  $\Delta_t = t_{new} - t_{old}$

$$q_1|_{new} - q_1|_{old} + S_2 (\Pi_u S_1 - S_2)^{-1} \partial_t q_{tot} \Delta_t = \int_{t_{old}}^{t_{new}} NL dt, \tag{3.12a}$$

$$h_{new} - h_{old} = \int_{t_{old}}^{t_{new}} \partial_x q_1 dt. \tag{3.12b}$$

The time evolution of the right-hand side terms in (3.12) is represented via the semi-implicit Crank–Nicolson approximation (Patankar 1980)

$$NL = NL|_{old} + \frac{t - t_{old}}{\Delta_t} \{NL|_{new} - NL|_{old}\}, \tag{3.13a}$$

$$\partial_x q_1 = \partial_x q_1|_{old} + \frac{t - t_{old}}{\Delta_t} \{\partial_x q_1|_{new} - \partial_x q_1|_{old}\}, \tag{3.13b}$$

and all spatial derivatives are approximated with central finite differences. Further, it is assumed in (3.12) that the model coefficients,  $S_i$ ,  $F_{ij}$ ,  $G_{ij}$ ,  $C_i$ ,  $J_i$ ,  $K_i$ ,  $L_i$  and  $M_i$  (evaluated at



$t_{old}$ ), as well as  $\partial_t q_{tot}$  are constant over the time step. The nonlinear operator  $NL|_{new}$  of the momentum equation at  $t_{new} = t_{old} + \Delta t$  is linearized in terms of the dependent variables,  $h = R - d$  and  $q_1$ , and their derivatives,  $h^{(j)}$  and  $q_1^{(i)}$

$$\begin{aligned}
 NL|_{new} = & NL|_{old} + \frac{\partial NL|_{old}}{\partial h^{(j)}} \{h^{(j)}|_{new} - h^{(j)}|_{old}\} \\
 & + \frac{\partial NL|_{old}}{\partial q^{(i)}} \{q^{(i)}|_{new} - q^{(i)}|_{old}\},
 \end{aligned}
 \tag{3.14}$$

where the bracketed superscripts denote the power of differentiation with respect to  $x$ . The thus obtained discretized evolution equations are evaluated at the  $N_x - 1$  points of an equidistant grid spanning from  $x = \Delta_x$  to  $x = \Lambda$  with grid spacing  $\Delta_x = \Lambda / (N_x - 1)$ . The point  $x = 0$  is excluded as it coincides with  $x = \Lambda$  due to streamwise periodicity. The periodicity conditions

$$h^{(j)}|_{x=0} = h^{(j)}|_{x=\Lambda}, \quad q^{(i)}|_{x=0} = q^{(i)}|_{x=\Lambda},
 \tag{3.15a}$$

are imposed directly, by making use of the nodes at and downstream of  $x = 0$  in the formulation of spatial derivatives at and upstream of  $x = \Lambda$ , and *vice versa*. We thus obtain a linear system of  $2(N_x - 1)$  algebraic difference equations with a cyclic pentadiagonal structure (Navon 1987) for the unknowns  $q_1|_{ix}$  and  $h|_{ix}$ . This system is solved through lower-upper (LU) decomposition at each time step, starting from the initial condition

$$d(x, t = 0) = d_0[1 + \epsilon_I \sin(2\pi x/\Lambda)], \quad q_1(x, t = 0) = q_{10}(q_{tot}(t = 0), d_0),
 \tag{3.16}$$

where  $\epsilon_I$  denotes the initial perturbation amplitude. Alternatively, the computation can be started from a TSS constructed with Auto07P, e.g. to study its stability.

The control parameters are  $\Lambda$ ,  $q_{tot}$  and the liquid volume  $V_1$

$$V_1 = \pi R^2 \Lambda \left\{ 1 - \frac{1}{2} \frac{d_0^2}{R^2} (2 + \epsilon_I^2) \right\}.
 \tag{3.17}$$

The total flow rate  $q_{tot}$  is either prescribed explicitly, or it results from an integral condition on the pressure drop (2.17). In the second case, (2.17) is recast to isolate  $\partial_t q_{tot}$

$$\begin{aligned}
 \partial_t q_{tot} \frac{1}{\Pi_u} \left\{ \int_0^L S_2 \frac{\Pi_u \tilde{S}_1 - \tilde{S}_2}{\Pi_u S_1 - \tilde{S}_2} dx - \int_0^L \tilde{S}_2 dx \right\} = & 2\Pi_\rho \Pi_u^2 \Delta p_2 - \int_0^L NLP(x, t) dx \\
 & + \int_0^L \left( \tilde{S}_1 - \frac{\tilde{S}_2}{\Pi_u} \right) NL(x, t) dx,
 \end{aligned}
 \tag{3.18}$$

where  $\partial_t q_1$  has been eliminated via (3.11) in the limit  $\Pi_{CRL} = 0$ , and then used to update  $q_{tot}$  at each time step

$$q_{tot}|_{new} = q_{tot}|_{old} + \partial_t q_{tot}|_{old} \Delta t.
 \tag{3.19}$$

Figure 4 represents results of a transient periodic computation for parameters according to figure 3. In particular, we have set  $V_1 / \pi / R^3 = 2.85$ , which lies far beyond the occlusion limit of TSS in figure 3(a). As shown in figure 4(b), our transient periodic computation, which was started from a virtually uniform film ( $\epsilon_I = 0.015$ ), evolves toward the TSS, represented here with a dashed blue profile and marked by a blue cross on the TPS branch in figure 3(a). Thus, we expect this branch to be representative of liquid plugs forming as a result of interfacial instability in a real system (comparisons with experiments are reported

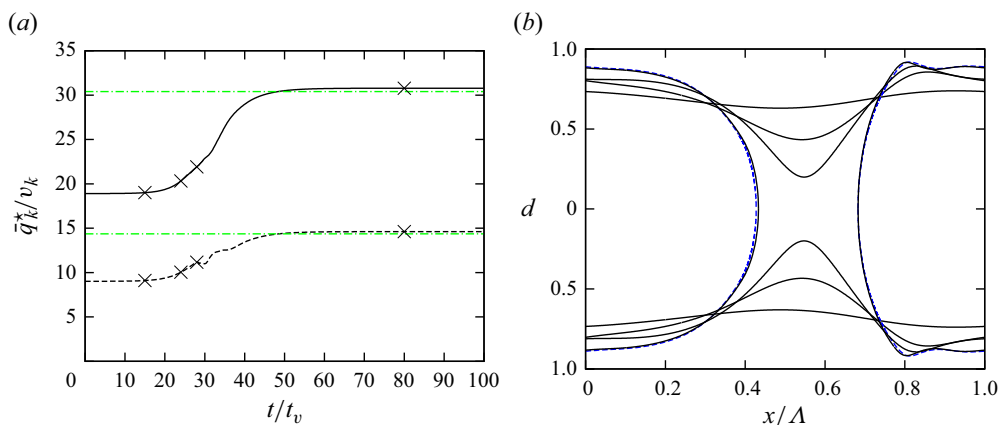


Figure 4. Transient periodic computation of a liquid plug forming from an initially quasi-uniform film. Parameters according to figure 3:  $V_1/\pi/R^3 = 2.85$ ,  $\epsilon_l = 0.015$ . (a) Time traces of the instantaneous Reynolds numbers,  $\bar{q}_k^*/\nu_k$ , with  $\bar{q}_k = \Lambda^{-1} \int_0^L q_k dx$ , in the liquid (solid) and gas (dashed). Dot-dashed green lines: final values for the DNS in figure 6(b); (b) profiles corresponding to crosses in panel (a) (solid) and to the TSS in figure 3(b) (dashed).

in § 4). The dot-dashed green curves in figure 4(a) correspond to the converged values for the instantaneous Reynolds numbers,  $\bar{q}_1^*/\nu_1$  and  $\bar{q}_2^*/\nu_2$ , obtained from our own transient periodic DNS (which will be introduced in figure 6b), using the solver Gerris (Popinet 2009). The time traces of  $\bar{q}_1^*/\nu_1$  and  $\bar{q}_2^*/\nu_2$  obtained from our transient periodic WRIBL computation (solid and dashed black curves) converge to these values (more comparisons with DNS are reported in § 4).

### 3.4. Open-domain computations

To represent the spatio-temporal evolution of liquid plugs, we apply the numerical procedure discussed in the previous section to an open domain with inlet and outlet conditions at  $x = 0$  and  $x = L$ . Inlet conditions are set by prescribing  $d$  and  $q_1$  at the first two grid points ( $i_x = 1, 2$ ) based on the primary flow

$$d|_{i_x=1} = d|_{i_x=2} = d_0, \tag{3.20a}$$

$$q_1|_{i_x=1} = q_1|_{i_x=2} = q_{10} [1 + F(t)]. \tag{3.20b}$$

The function  $F(t)$  in (3.20b) allows us to apply a tailored inlet forcing

$$F(t) = \epsilon_1 \sin(2\pi f t) + \epsilon_2 \sum_{k=1}^N \sin(2\pi k \Delta f t + \varphi_{rand}), \quad \Delta f = 2f_c/N. \tag{3.21}$$

The first term constitutes a harmonic perturbation of frequency,  $f$ , and the second one mimics white noise through a series of  $N = 1000$  Fourier modes that are shifted by a random phase shift,  $\varphi_{rand} = \varphi_{rand}(k) \in [0, 2\pi]$ , and that span a frequency range of twice the linear cutoff frequency,  $f_c$  (Chang, Demekhin & Kalaidin 1996). All our computations were run with the same  $\varphi_{rand}(k)$  number series, which was generated once and for all with the pseudo-random number generator RandomReal in Mathematica (2014). The strength of the two terms in (3.21) is determined through their amplitudes,  $\epsilon_1$  and  $\epsilon_2$ . When  $\epsilon_1 = 0$ ,

the inlet perturbation consists of only white noise. This setting will be used to simulate the noise-driven formation of liquid plugs, as it would occur in an experiment.

At the outlet, we apply boundary conditions inspired by those of Richard, Ruyer-Quil & Vila (2016), which ensure that liquid is always sufficiently drained from the domain, by introducing two downstream ghost nodes at  $i_x = N_x + 1$  and  $i_x = N_x + 2$

$$d|_{i_x=N_x+1} = d|_{i_x=N_x+2} = d|_{i_x=N_x}, \quad (3.22a)$$

$$q_1|_{i_x=N_x+1} = q_{10} \frac{q_{10}^{PG}(d|_{i_x=N_x})}{q_{10}^{PG}(d_0)}, \quad (3.22b)$$

where  $q_{10}^{PG}(d) = q_{10}(\Pi_\rho = \Pi_\mu = 0, d)$  is the passive-gas limit of the primary flow rate  $q_{10}$  for a given  $d$ , which is known analytically. Our computations are started from the initial condition

$$d(x, t = 0) = d_0, \quad q_1(x, t = 0) = q_{10}. \quad (3.23)$$

We point out that no information for the interface height in the second downstream ghost cell ( $d|_{i_x=N_x+2}$  in our case) was given in Richard *et al.* (2016). Our choices for  $d|_{i_x=1}$  (3.20) and  $d|_{i_x=N_x+2}$  (3.22) were guided by numerical convenience. The twice removed ghost cells only affect the discretized form of the third derivative,  $\partial_{xxx}d$ , which is negligible at the inlet. At the outlet, the flow is dominated by the imposed flow rate,  $q_1|_{i_x=N_x+1}$ , and, thus, the effect of  $d|_{i_x=N_x+2}$  is weak.

#### 4. Validation vs DNS and experiments

We validate our approach for computing liquid plugs by confronting our WRIBL model (2.13) with experiments and DNS. We start with the configuration from figure 3(a), which corresponds to silicone oil II in table 1, subject to an aerostatic pressure drop ( $M = 1$ ). Figure 5 represents TSS in terms of two important measures, i.e. the plug speed,  $c$ , and the gas Reynolds number,  $Re_2$ , which quantifies the entrained gas flow rate. As discussed in figure 3(a), liquid-plug solutions lie beyond LP1 on the solid blue curves in figure 5(a,b), which represent our WRIBL predictions. The green squares in the same graphs mark data points obtained via transient periodic DNS with Gerris (see Dietze *et al.* (2020) for details of such runs), evidencing very good agreement with the WRIBL model. For the low-viscosity liquid considered here,  $Re_1$  is quite large, and, thus, inertia is not negligible. This is evidenced by the substantial difference (approximately 25 %) between our full-model predictions (solid blue curves) and the black dashed curves, which represent the inertialess limit of our WRIBL model ( $S_k = F_{kj} = G_{kj} = 0$  in (2.13)).

Figure 6 shows streamlines in the moving reference frame for one of the liquid-plug solutions from figure 5 ( $V_l/\pi/R^3 = 2.85$ ), as obtained from our WRIBL model (figure 6a) and our DNS (figure 6b). Our model captures all relevant flow features, in particular the toroidal vortex within the liquid plug (Ubal *et al.* 2008) and the three main toroidal vortices within the gas bubble. The shape of the liquid–gas interface is predicted accurately in the thin portion of the liquid film, whereas agreement deteriorates in the steepest parts of the leading and trailing fronts of the liquid plug. In these regions, the spherical-cap approximation (2.14) allows us to recover good agreement (dashed green lines).

In figure 7(a), the solid black line represents the thus reconstructed liquid–gas interface for the system in figure 6 (crosses mark patching points), evidencing good agreement with the DNS profile (green line with open circles). The other three panels in figure 7 compare spatial profiles of different quantities related to the stress field at the tube wall. We start

Fluids	$\rho$ (kg m <sup>-3</sup> )	$\mu$ (Pa s)	$\sigma$ (N m <sup>-1</sup> )	$Ka$	Reference
silicone oil I	970	12.9	0.0215	$3.3 \times 10^{-3}$	Camassa <i>et al.</i> (2014)
silicone oil II	900	$4.5 \times 10^{-3}$	0.020	121.4	Piroird, Clanet & Quéré (2011)
glycerol(89 %)-water	1223.9	0.167	0.065	3.5	Dao & Balakotaiah (2000)
mucus I	1000	$13 \times 10^{-3}$	0.020	30.6	Muradoglu <i>et al.</i> (2019)
air I	1.2	$1.8 \times 10^{-5}$	—	—	—

Table 1. Properties of the fluids used in our computations. The Kapitza number,  $Ka$ , is defined as  $Ka = \sigma/(\rho_1 g^{1/3} \nu_1^{4/3})$ , where  $\sigma$ ,  $\rho_1$  and  $\nu_1$  denote the surface tension and the density and kinematic viscosity of the liquid, and  $g = 9.81 \text{ m s}^{-2}$  designates the gravitational acceleration.

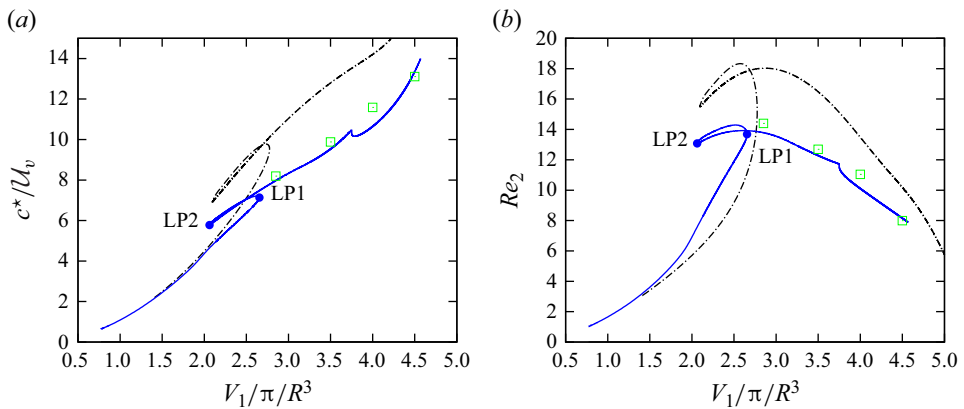


Figure 5. The TSS from figure 3 (curves) compared with our own DNS (symbols) using Gerris (Popinet 2009):  $Ka = 121.4$ ,  $R^* = 1.5 \text{ mm}$ ,  $M = 1$ ,  $\Lambda = 5.4$ . Solid blue curve: full model (2.13), dot-dashed black curve: inertialess limit ( $S_k = F_{kj} = G_{kj} = 0$ ). (a) Plug celerity  $c$ ; (b) gas Reynolds number,  $Re_2$ , quantifying the gas flow rate transported by the gas bubbles in between two liquid plugs.

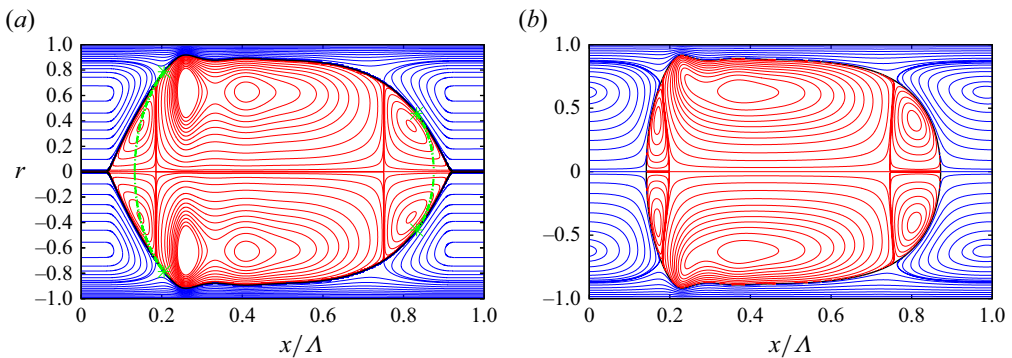


Figure 6. The TPS forming in a vertical cylindrical tube. Streamlines in the reference frame moving with the plug speed,  $c$ . Parameters according to figure 3(a):  $\Lambda = 5.4$ ,  $V_1/\pi/R^3 = 2.85$ ,  $M = 1$ . (a) Transient periodic computation with our augmented WRIBL model (2.13):  $Re_1 = 30.8$ ,  $Re_2 = 14.6$ ,  $c^* = 0.31 \text{ m s}^{-1}$ . Dashed green lines correspond to spherical-cap approximation (2.14) between patching points (marked by green asterisks), using  $\varepsilon^{max} = 0.75$ ; (b) periodic DNS with Gerris:  $Re_1 = 30.4$ ,  $Re_2 = 14.4$ ,  $c^* = 0.30 \text{ m s}^{-1}$ .

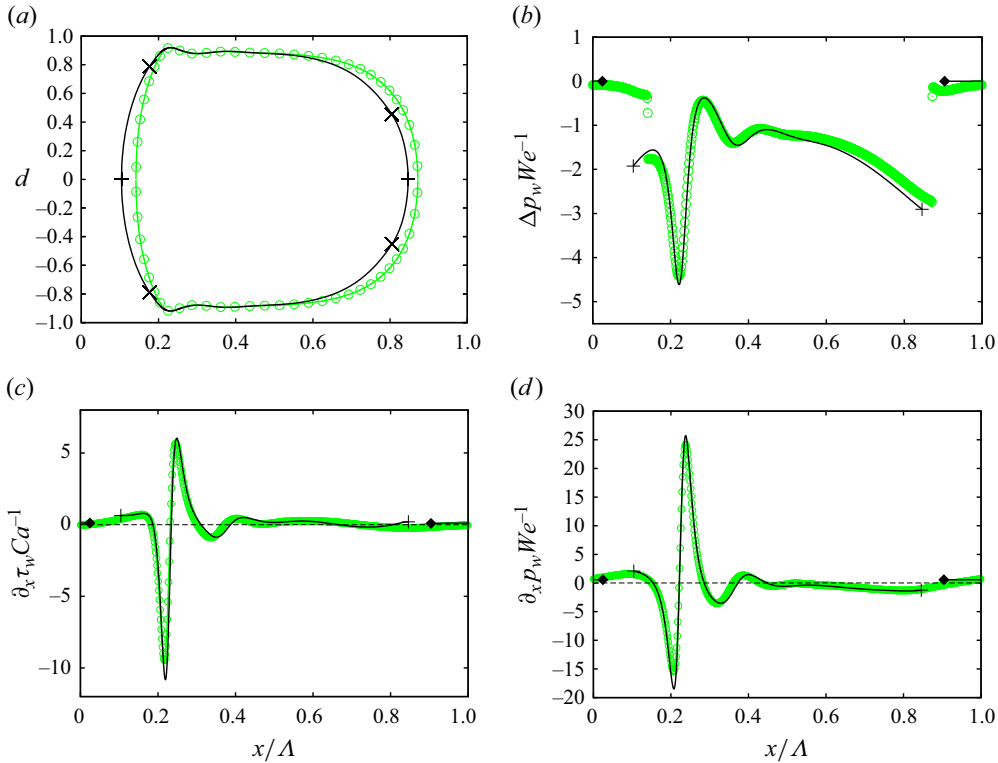


Figure 7. Liquid stresses at the tube wall,  $r = 1$ , within a TPS. Parameters according to figure 6. Open green circles: DNS; solid black lines: WRIBL model. (a) Liquid–gas interface, showing gas bubble in between two liquid plugs; (b) pressure difference across the tube,  $\Delta p_w$  (4.1); (c) axial wall shear stress derivative,  $\partial_x \tau_w$ , according to (4.2b); (d) axial wall pressure derivative,  $\partial_x p_w$ , according to (4.2a). Crosses mark patching points for spherical-cap reconstruction (2.14), using  $\epsilon^{max} = 0.75$ , plus signs mark apex of spherical cap and diamonds mark limits of pseudo-plug.

with the excess pressure  $\Delta p_w$

$$\Delta p_w = \frac{\Delta p_w^*}{\rho_1 U_1^2}, \quad \Delta p_w^* = p^*|_{r^*=R^*} - p^*|_{r^*=0}, \quad (4.1)$$

which is obtained by integrating (2.1b), substituting (2.8), truncating at order  $\mathcal{O}(\epsilon^2)$ , introducing (2.10b) and setting  $\epsilon = 1$ . As shown in figure 7(b), our WRIBL model (solid curves) accurately predicts both the  $\Delta p_w$  profile and its maximum absolute value compared with the DNS (open green circles). The segment between the apex of the spherical cap (marked by plus sign) and the start of the pseudo-plug (marked by filled diamond) is not drawn, as it has no physical meaning.

Experiments of Kay *et al.* (2004) and Tavana *et al.* (2011) have shown that liquid-plug-induced epithelial cell damage is controlled by the magnitude of the axial derivatives of wall pressure,  $p_w$ , and wall shear stress,  $\tau_w$

$$\partial_x p_w = \partial_x [p_1]_{r=1} = Re_1^{-1} \left[ \frac{1}{r} \partial_r (r \partial_r u_1) \right]_{r=1} + Fr^{-1}, \quad (4.2a)$$

$$\tau_w = \partial_r u_1|_{r=1}, \quad \partial_x \tau_w = \partial_x [\partial_r u_1]_{r=1}, \quad (4.2b)$$

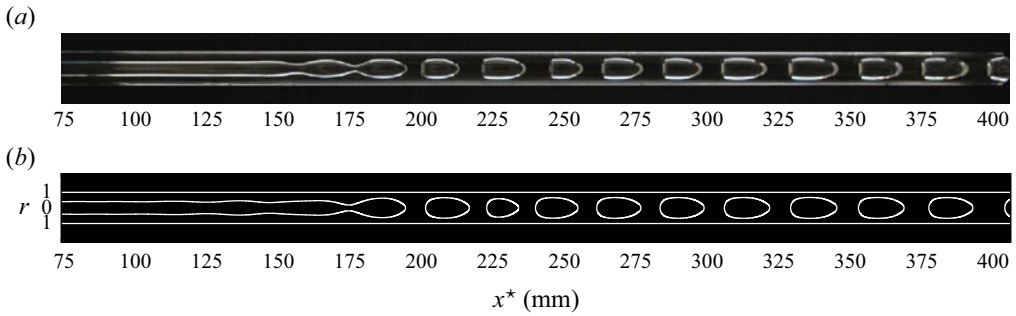


Figure 8. Highly viscous falling liquid film in contact with air:  $Ka = 3.3 \times 10^{-3}$  (silicone oil I, air in table 1),  $R^* = 5$  mm,  $Re_1 = 4.5 \times 10^{-4}$ ,  $M = 1$ . (a) Experiment from figure 3(c) of Camassa *et al.* (2014), reproduced here with permission from Cambridge University Press. (b) Open-domain WRIBL computation (true to scale) using inlet noise (3.21):  $\epsilon_1 = 0$ ,  $\epsilon_2 = 10^{-4}$ . Leading and trailing portions of the liquid plugs were reconstructed with the spherical-cap approximation (2.14), using  $\epsilon^{max} = 0.68$ .

where (4.2a) is obtained by evaluating (2.1a) at  $r = 1$  (and setting  $\varepsilon = 1$ ), and where  $u_1$  is reconstructed according to (2.8), using (2.10a) and (2.19), which ensures consistency at order  $\mathcal{O}(\varepsilon^2)$ . Figure 7(c,d) plots profiles of  $\partial_x \tau_w$  and  $\partial_x p_w$  obtained from our WRIBL model (solid curves) based on (4.2b) and (4.2a), in comparison with our DNS predictions (green curves with open circles). Our WRIBL model predicts the spatial variation and the maximum magnitude of both quantities, in good agreement with the DNS.

All three quantities,  $\Delta p_w$  (figure 7b),  $\partial_x \tau_w$  (figure 7c) and  $\partial_x p_w$  (figure 7d), exhibit pronounced extrema around the first capillary trough preceding the leading front of the liquid plug. Also,  $\partial_x \tau_w$  and  $\partial_x p_w$  change sign over a very short length scale in this region, implying a temporally oscillatory stress field during the passage of a liquid plug. Spatio-temporal variations increase the potential of mechanical damage to epithelial cells in the pulmonary airways (Romano *et al.* 2021). In § 5.2, we will use our WRIBL predictions obtained from (4.1), (4.2b) and (4.2a), and the corresponding time derivatives,  $\partial_t \tau_w = -c \partial_x \tau_w$  and  $\partial_t p_w = -c \partial_x p_w$ , to assess the potential for epithelial cell damage linked to TPS under representative flow conditions in the conducting zone of the tracheobronchial tree.

Further validation of our WRIBL model (2.13) is provided in figure 8, where we have reproduced numerically the experiment in figure 3(c) of Camassa *et al.* (2014), who studied liquid-plug formation in a narrow vertical tube, using a high-viscosity liquid (silicone oil I in table 1) in contact with air.

Our WRIBL computation (figure 8b) was performed on an open domain, applying the noisy inlet perturbation (3.21) to mimic experimental noise. Occlusion in the present case occurs according to scenario I in Dietze *et al.* (2020), i.e. the liquid Reynolds number,  $Re_1 = 4.5 \times 10^{-4}$ , lies beyond the LP of the linearly most-amplified TWS, and liquid plugs form as a result of surface waves emerging from linear wave selection. This limit point is marked by LP1 in figure 9(a), which represents TSS at  $f = f_{max}$ , where  $f_{max}$  denotes the spatially most-amplified frequency obtained from linear stability analysis. Comparing the upper panel (experiment) and lower panel (WRIBL) in figure 8, we conclude that our model correctly represents this occlusion regime. In particular, the spatial evolution of precursory surface waves, their pinch-off to form liquid plugs (subsequently convected downstream) and the number and shape of these plugs, are predicted quite well.

## Liquid plugs in narrow tubes

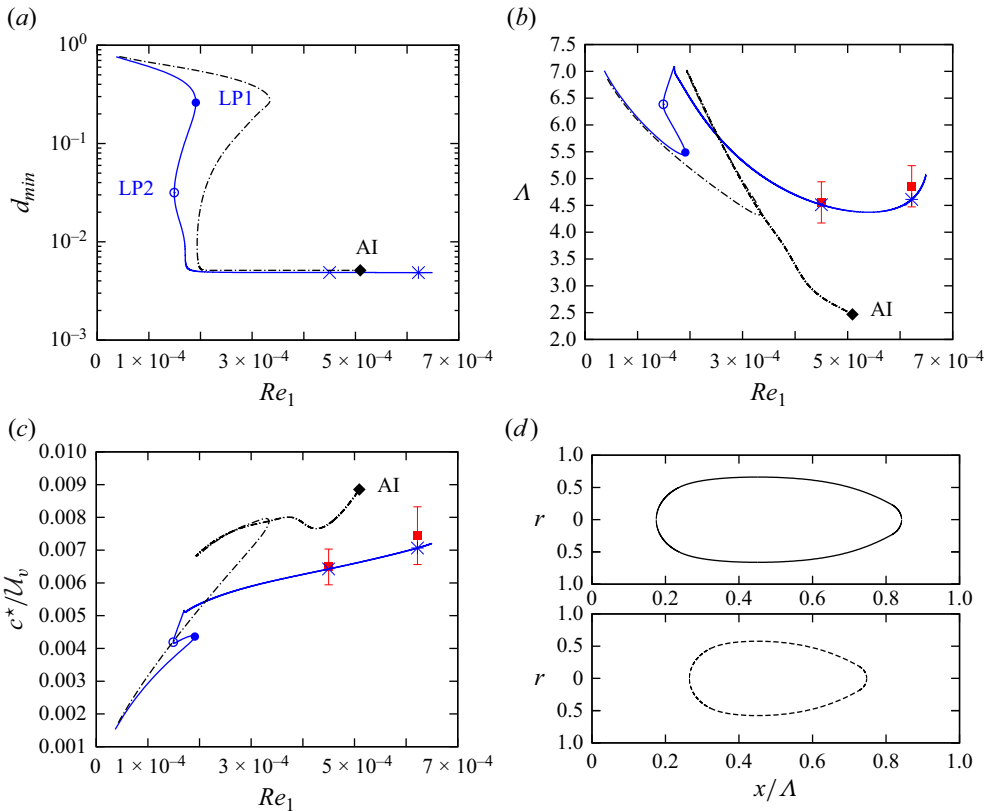


Figure 9. The TSS at  $f = f_{max}$  and  $M = 1$  obtained with our WRIBL model (2.13) for the configuration in figure 8. Solid blue curves with circles: full model; dot-dashed black:  $J_k = K_k = L_k = M_k = 0$  in (2.13). Filled black diamonds mark AI limit. Lower branch beyond LP2 in panel (a) corresponds to TPS, which are compared with experiments (filled red squares) from figures 3(c) ( $Re_1 = 4.5 \times 10^{-4}$ ) and 3(d) ( $Re_1 = 6.22 \times 10^{-4}$ ) of Camassa *et al.* (2014). (a) Minimal core radius; (b) wavelength; (c) wave/plug speed; (d) plug profiles corresponding to cross and asterisk in panels (a–c). Solid:  $Re_1 = 4.5 \times 10^{-4}$ ,  $f_{max}^* = 0.145$  Hz; dashed:  $Re_1 = 6.22 \times 10^{-4}$ ,  $f_{max}^* = 0.155$  Hz.

Further, we show in figure 9 that several liquid-plug measures from the experiment can be predicted accurately based on TSS at  $f = f_{max}$  obtained with our WRIBL model. Both the wavelength,  $\Lambda$  (combined length of liquid plug and gas bubble), represented in figure 9(b), and the plug speed,  $c = \Lambda f_{max}$ , represented in figure 9(c), lie within the experimental error bars (experimental points are marked by filled squares), which were determined graphically from the variation of  $\Lambda$  between different plug/bubble pairs in figure 3(c) of Camassa *et al.* (2014). Crosses and asterisks on the TSS branches in figure 9(a–c) mark the experimental conditions corresponding to figure 3(c,d) in Camassa *et al.* (2014), whereby the former figure is reproduced here in figure 8(a).

The dot-dashed black curves in figure 9(a–c) represent TSS obtained in the absence of axial viscous diffusion, i.e. when setting  $J_k = K_k = L_k = M_k = 0$  in (2.13). In this limit, agreement with the experiments is greatly deteriorated. Thus, accounting for axial viscous diffusion, by developing our WRIBL model up to order  $\epsilon^2$ , has proven necessary in order to accurately capture liquid plugs of highly viscous liquids.

Finally, we point out that our open-domain computation in figure 8(b) was run with an imposed total flow rate  $q_{tot}$ , corresponding to the TPS at  $M = 1$  in figure 9(a). For this

high-viscosity working liquid, gas–liquid coupling is very weak ( $\Pi_\mu = 1.4 \times 10^{-6}$ ) and thus imposing  $M = 1$  via (2.17) requires a very fine grid resolution around the liquid plug, which is prohibitive in open-domain computations.

### 5. Results: application to airway occlusion

We apply our WRIBL model (2.13) to study liquid-plug formation by a mucus film lining the inner surface of a respiratory airway. We assume a mucus rheology corresponding to healthy conditions, where neither viscoelasticity (Choudhury *et al.* 2023) nor shear thinning (Chatelin *et al.* 2017) play a significant role. In particular, our computations are based on a Newtonian model mucus according to Muradoglu *et al.* (2019), i.e. mucus I in table 1. For the gas phase, we assume ambient air, i.e. air I in table 1.

We focus on the conducting zone of the human respiratory network, i.e. the first 16 airway generations according to the lung architecture model of Weibel & Gomez (1962)

$$R^* = R_{Weib}^* = R_0^* 2^{-(n/3)}, \tag{5.1a}$$

$$L^* = L_{Weib}^* = L_0^* 2^{-(n/3)}, \tag{5.1b}$$

$$Re_2 = Re_2^{Weib} = Re_{20} 2^{-(2/3)n} = \frac{Q_{20}^*}{\pi R_0^* v_2} 2^{-(2/3)n}, \tag{5.1c}$$

where  $n$  denotes the airway generation,  $R^*$  and  $L^*$  the radius and length of the airway,  $Q_2^*$  and  $Re_2$  the corresponding gas flow rate and gas Reynolds number and the subscript 0 refers to the trachea, i.e.  $n = 0$ , for which we set  $R_0^* = 9$  mm and  $L_0^* = 120$  mm, according to a typical adult (Weibel & Gomez 1962).

In the current manuscript, we do not account for the time variation of the air flow rate during the breathing cycle. Instead, we set a time-constant tracheal gas flow rate, which is based on the reference value  $Q_{20}^* = \pm V_T^* f_T^* = \pm 2.5 \times 10^{-4} \text{ m}^3 \text{ s}^{-1}$ , with a tidal volume,  $V_T^* = 500 \times 10^{-6} \text{ m}^3$ , and a tidal frequency,  $f_T^* = 0.5$  Hz, according to typical settings for assisted ventilation (Halpern *et al.* 1998), yielding  $Re_{20} = \pm 590$ . Based on this, the gas flow is always laminar for generations  $n > 2$ , and we restrict our investigation to this range, as our WRIBL model does not account for turbulence.

The sign of  $Q_{20}^*$  and  $Re_{20}$  allows us to distinguish between situations where the gas flow is oriented in the direction of gravity ( $Q_{20}^*, Re_{20}^* > 0$ ) or opposite to gravity ( $Q_{20}^*, Re_{20}^* < 0$ ). We will designate these as co-current and counter-current configurations throughout. Due to the branching nature of the lung architecture, two airways of the same generation can be oriented in opposite directions, and, thus, the co- and counter-current configurations can occur both during expiration and inspiration. Of course, the direction of the gas flow is relevant only when gravity plays a role, and we will show that this is the case here. Strictly speaking, our WRIBL model, which is based on an axisymmetric formulation (2.13), is valid only for airways aligned with gravity, and we will focus on this situation. Thus, we cannot account for cross-stream gravity, which can lead to asymmetric liquid distribution about the airway equator (Suresh & Grothberg 2005). For this, a full three-dimensional model is required.

Further, we neglect the effect of beating cilia lining the airway walls, which are responsible for mucociliary clearance (Spagnolie 2015), as well as the periciliary liquid (PCL) in which they are immersed. These effects are assumed to be negligible for conditions in the vicinity of liquid-plug formation. For reference, the thickness of the PCL layer is  $h_{PCL}^* \sim 8 \mu\text{m}$  for  $n = 16$ , i.e.  $h_{PCL}^*/R \sim 4 \%$ . Finally, we assume the inner surface of the airways to be perfectly cylindrical.



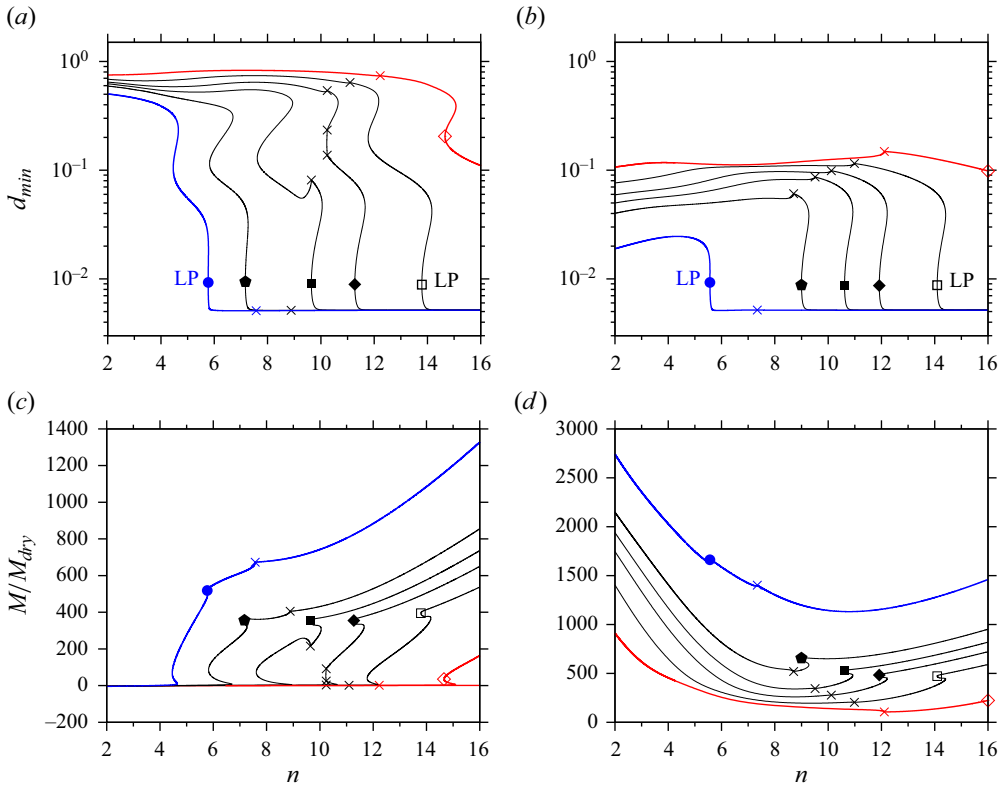


Figure 10. Airway occlusion under imposed gas flow rate for different  $h_{VE}$ . Linearly most-dangerous TSS vs airway generation  $n$  based on lung architecture (5.1) of Weibel & Gomez (1962):  $Ka = 30.6$  (mucus I and air I in table 1),  $Re_{20} = \pm 590$ ,  $k = k_{max}$ ,  $R^* = R_{Weib}^*$ ,  $Re_2 = Re_2^{Weib}$ . Crosses mark transition between CI, where  $\omega_i = \partial_{\omega} k_i = 0$  is imposed (3.9a), and AI, where  $d\omega/dk = 0$  (with  $k, \omega \in \mathbb{C}$ ) is imposed (3.9b). Filled circles to open diamonds:  $h_{VE} = 0.4, 0.3, 0.267, 0.24, 0.2$  and  $0.15$ . (a,c) Co-current configuration:  $Re_{20} = 590$ ,  $M_{dry} < 0$ ; (b,d) counter-current configuration:  $Re_{20} = -590$ ,  $M_{dry} > 0$ . (a,b) Minimum core radius; (c,d) normalized pressure drop, where  $M_{dry}$  (5.3) corresponds to dry airways ( $h_{VE} = 0$ ).

### 5.1. Liquid-plug formation based on TSS

We apply the numerical continuation procedure introduced in § 3.2 to advance TSS in terms of the airway generation  $n$  (see e.g. figure 10). For this, we assume that all quantities evolve continuously with  $n$  (Halpern *et al.* 1998), based on the lung architecture model (5.1) of Weibel & Gomez (1962). In particular, we are interested in predicting the transition from TWS to TPS, which allows us to identify in what airway generation liquid plugs may arise. In generations where TPS do not exist, plug formation is highly unlikely, even in a transient setting. In addition to the airway generation,  $n$ , there is one other free control parameter in our problem, for which we choose the liquid holdup,  $h_{VE} = h_{VE}^*/R^*$

$$h_{VE} = 1 - d_{VE}, \tag{5.2}$$

which controls the thickness of the mucus film. This parameter can increase significantly in the case of mucus overproduction or impeded mucociliary clearance caused by respiratory diseases (Fahy & Dickey 2010).

In our calculations, we track the linearly most-dangerous TSS by setting  $k = k_{max}$ , where  $k_{max}$  is the most-dangerous wavenumber, as obtained by simultaneously solving the linear stability problem (3.9). Thus, for each airway generation, we obtain the TSS most likely

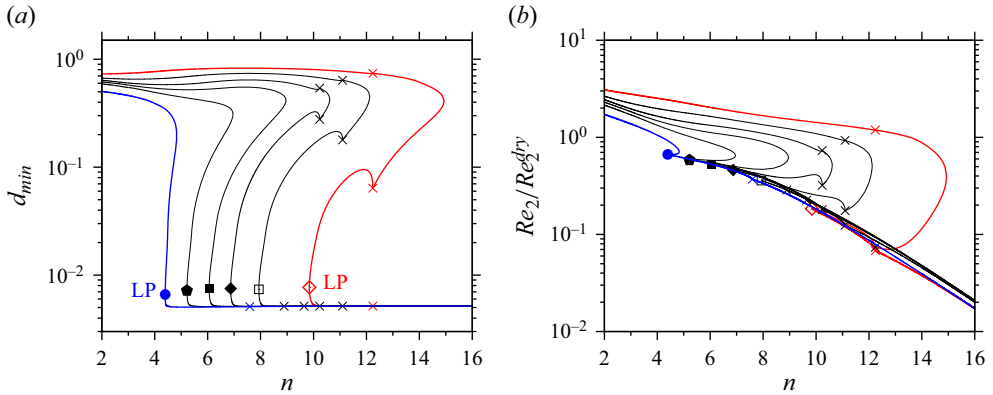


Figure 11. Airway occlusion under imposed pressure drop for different values of the liquid holdup,  $h_{VE}$ . Linearly most-dangerous TSS vs airway generation,  $n$ , based on lung architecture (5.1) of Weibel & Gomez (1962):  $Ka = 30.6$  (mucus I and air I in table 1),  $M/M_{dry} = 20$ ,  $Re_{20}^{dry} = 590$  ( $M_{dry} < 0$ ),  $k = k_{max}$ ,  $R^* = R_{Weib}^*$ . Filled circles to open diamonds:  $h_{VE} = 0.4, 0.3, 0.267, 0.24, 0.2$  and  $0.15$ . (a) Minimum core radius; (b) normalized gas Reynolds number.  $M_{dry}$  (5.3) and  $Re_2^{dry}$  correspond to dry airways ( $h_{VE} = 0$ ) in the absence of gravity ( $Fr^{-1} = 0$ ). The LPs mark onset of TPS. Crosses mark transition between CI, where  $\omega_i = \partial_\omega k_i = 0$  is imposed (3.9a), and AI, where  $d\omega/dk = 0$  (with  $k, \omega \in \mathbb{C}$ ) is imposed (3.9b).

to emerge in a real system, and we have checked that the corresponding most dangerous wavelength,  $\Lambda_{max} = 2\pi/k_{max}$ , satisfies  $\Lambda_{max} \leq L_{Weib}$ , i.e. that the most-dangerous TSS fits into the typical length of the considered airway generation (see figure 12, which will be introduced later). Further, our spatio-temporal stability formulation introduced in § 3.2 allows us to distinguish between: (i) CI, where we set  $\omega_i = \partial_\omega k_i = 0$  via (3.9a), and  $k_{max}$  corresponds to the linear mode with maximum spatial growth rate, and (ii) AI, where we set  $d\omega/dk = 0$  via (3.9b), and  $k_{max}$  corresponds to the absolute mode, i.e. a perturbation growing in time at fixed axial position,  $x$ . The TPS in the AI regime are particularly dangerous, as the linear perturbation in that case cannot be advected out of the airway, and plug formation is thus more likely in a transient setting. Therefore, the CI/AI transition is highlighted by crosses in all figures of the current section, i.e. figures 10–16.

Figure 10 represents TSS vs the airway generation  $n$  for imposed  $R^* = R_{Weib}^*$  and  $Re_2 = Re_2^{Weib}$ , according to (5.1), for different values of the liquid hold up,  $h_{VE}$ . Here, we confront the co-current ( $Re_{20} = 590$ , figure 10a,b) and counter-current ( $Re_{20} = -590$ , figure 10c,d) configurations. Figure 10(a) represents TSS in terms of the minimum core radius,  $d_{min}$  (solid curves). Upon decreasing  $h_{VE}$  (from  $h_{VE} = 0.4$  to  $h_{VE} = 0.2$ ), the critical generation for TPS formation (LPs, marked by symbols) shifts significantly toward distal airways (from  $n = 6$  to  $n = 14$ ). At the same time, the CI/AI transition (marked by crosses) increasingly shifts from the TPS branch to the TWS branch, making liquid-plug formation in a transient setting more and more likely. In particular, for  $h_{VE} \leq 0.267$ , the entire TPS branch lies in the AI regime. We point out that the observed multiplicity of TSS at fixed  $h_{VE}$  and  $n$  is similar to the one discussed in figure 3(a). It is quite probable that the TWS on the intermediate branches between the upper LP and the TPS are unstable here as well. To check this rigorously, the approach of Camassa *et al.* (2021) for investigating the stability of TWS needs to be applied to the continuation results in figure 10(a), where the continuation parameter is different. This is outside the scope of the current manuscript.

According to figure 10(c), the TPS from figure 10(a) are associated with a spectacular increase of the normalized gas pressure gradient,  $M$  (2.18), vs its reference value,  $M_{dry}$ , for

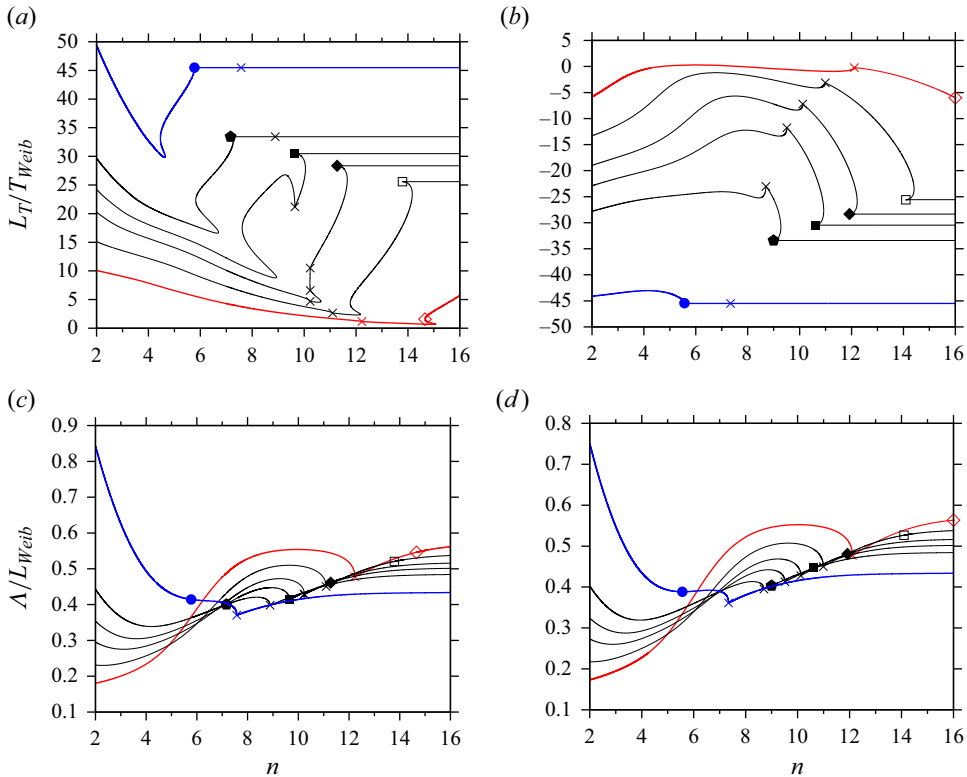


Figure 12. Length scales of TSS from figure 10, as compared with the airway length,  $L_{Weib}$  (5.1). (a,b) Relative distance of propagation,  $L_T/L_{Weib}$ , during half of one breathing period,  $1/f_T$ , where  $L_T = c/2f_T$ ; (c,d) relative wavelength,  $\Delta/L_{Weib}$ . (a,c) Co-current:  $Re_{20} = 590$ ; (b,d) counter-current:  $Re_{20} = -590$ .

dry gravity-free airways

$$M_{dry} = \lim_{\substack{d \rightarrow R \\ 1/Fr \rightarrow 0}} \{\partial_x p_2^*\} \frac{1}{\rho_2 g} = -8 \frac{Re_2}{Ga_2}, \quad Ga_2 = \frac{R^{*3} g}{v_2^2}, \quad (5.3)$$

where  $Ga_2$  denotes the gas Galileo number. Conversely, when  $M/M_{dry}$  is imposed instead of  $Re_{20}$ , as shown in figure 11, occlusion leads to a virtual halt of the gas flow through the affected airway, as demonstrated via the  $Re_2$  vs  $n$  plot in figure 11(b), where we have fixed  $M/M_{dry} = 20$  based on  $Re_{20}^{dry} = 590$  ( $M_{dry} < 0$ ), keeping all other parameters as in figure 10(a). Indeed, when moving from the upper TWS branches to the TPS branches at constant  $n$  in figure 11(b),  $Re_2$  drops by one order of magnitude. This underlines the extremely noxious implications of airway occlusion for the proper operation of the respiratory tract.

We turn now to figure 10(b,d), which represents TSS for the same parameters as in figure 10(a,c), but for the counter-current configuration. Comparing figure 10(a,b), we see that the critical  $n$  for airway occlusion shifts by one or two generations between the co- and counter-current configurations. Based on this, we may conclude that gravity affects the occlusion limit up to generation  $n = 10$ , where  $Bo = \rho_1 g R^{*2} / \sigma \sim 0.4$ . This relatively small gravitational effect is contrasted by the spectacular difference in the core radius,  $d_{min}$ , for the TWS branches associated with these two configurations. While TWS do not

significantly obstruct the airways for the co-current configuration (figure 10a),  $d_{min}$  attains values that are smaller by one order of magnitude for the counter-current configuration (figure 10b). As shown in figure 10(d), this translates to extremely large gas pressure drops, even before the onset of TPS. Thus, in contrast to the co-current configuration, breathing in the counter-current configuration can be drastically impaired even in the absence of liquid-plug formation.

In figure 12, we characterize different length scales associated with the TSS obtained in figure 10 vs the airway generation,  $n$ , by comparing them with the airway length,  $L_{Weibel}$  (5.1). Figure 12(a,b) represent the distance,  $L_T = c/2/f_T$ , which a TSS would travel during one half of the breathing cycle, i.e.  $2/f_T$ , where  $c$  is the nonlinear TSS speed. Both for the co-current configuration (figure 12a) and for the counter-current configuration (figure 12b), TPS are associated with very large values of  $|L_T|/L_{Weibel}$ . This implies that liquid plugs can easily propagate into more distal airways, thus exacerbating the noxious implications of airway occlusion. Of course,  $Re_2$  is not constant in time during a real breathing cycle, and thus our predictions in figure 12(a,b) provide only a conservative estimate.

In figure 12(c,d), we compare the wavelength,  $\Lambda$ , of the TSS from figure 10(a,b) with the corresponding airway length,  $L_{Weibel}$ . First of all, we observe that  $\Lambda < L_{Weibel}$  is satisfied across the first 16 airway generations, implying that at least one TSS fits into every airway. At small  $n$ , where TWS prevail, that number can increase to five. At large  $n$ , where TPS prevail, we observe approximately two liquid plugs per airway, independent of the liquid holdup  $h_{VE}$ . Thus, nonlinear interactions between liquid plugs may need to be accounted for when modelling the dynamics of airway occlusion.

Figure 13 compares the liquid volume,  $V_1$ , of the TSS in figure 10(a) with two thresholds corresponding to static equilibrium shapes that do not fully wet the inner surface of the airway. Quasi-static conditions can occur when the gas flow rate becomes zero in between the inspiration and expiration strokes, provided the effect of gravity is negligible. Firstly, figure 13(a) compares  $V_1$  with the threshold,  $V_U$  (Everett & Haynes 1972), for the formation of liquid unduloids (Delaunay 1841)

$$V_U = 1.73\pi R^3. \tag{5.4}$$

Unduloids are always shorter than the most-amplified wavelength of the classical Plateau–Rayleigh instability, and, thus, inevitably lead to a dewetting of the liquid film for  $V_1 \leq V_U$ , as a result of the subcritical nature of the instability. Figure 13(a) shows that  $V_1 \leq V_U$  can indeed occur within the airways, i.e. for  $n < 7$  and  $h_{VE} \leq 0.24$ . However, the corresponding Bond number,  $Bo_U = \rho_1 g h_{VE}^2 / \sigma$ , which is plotted in figure 13(c), indicates that quasi-static conditions can be reached only for  $n > 5$ , where  $Bo_U < 0.1$ , at least for the considered values of  $h_{VE}$ . Widespread conditions for dewetting due to unduloid formation are limited to much smaller values of  $h_{VE}$ , but the growth rate of the Plateau–Rayleigh instability may be very small there, vs the frequency of the breathing cycle.

Secondly, figure 13(b) compares  $V_1$  with the threshold,  $V_P$ , for the existence of fully wetting static spherical liquid plugs

$$V_P = \pi R^3 \left\{ \Lambda - \frac{4}{3} \right\}, \tag{5.5}$$

and we see that all represented TSS satisfy  $V_1/V_P < 1$ . Assuming that quasi-static conditions can be reached over the course of the breathing cycle, dewetting due to plug formation is thus possible in all airway generations. However, according to figure 13(d), which represents the corresponding Bond number,  $Bo_P = Bo = \rho_1 g R^2 / \sigma$ , such conditions are limited to the most distal airways, i.e.  $n > 13$ , where  $Bo_P < 0.1$ .

## Liquid plugs in narrow tubes

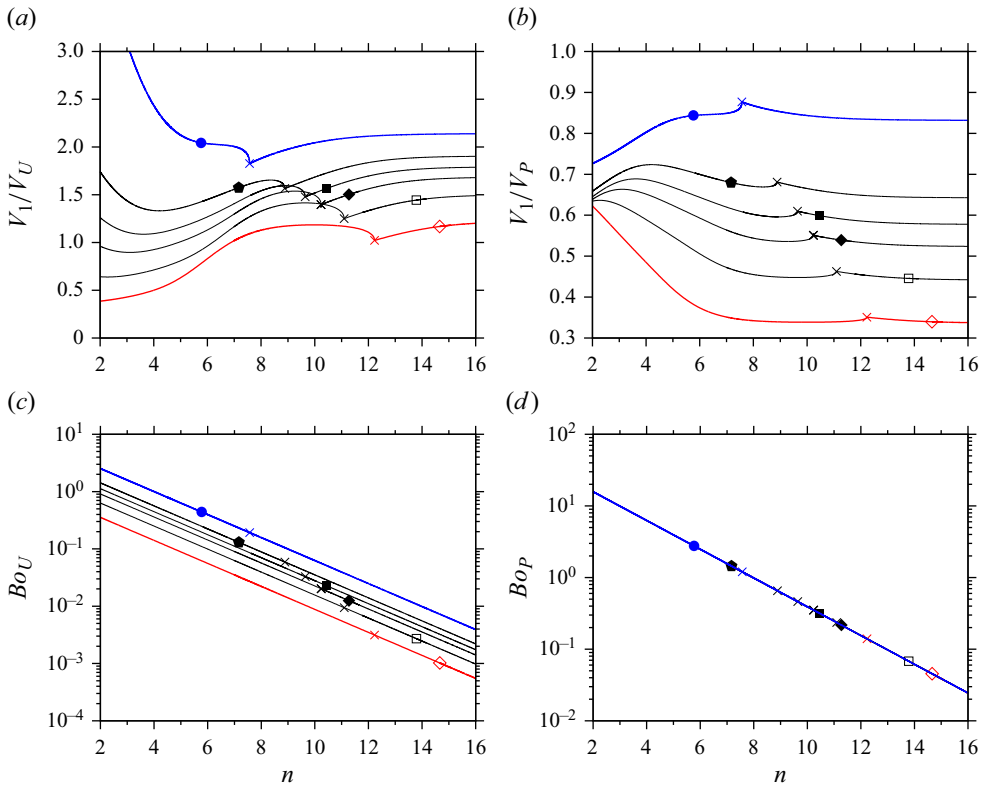


Figure 13. Liquid volume,  $V_1$ , of TSS in figure 10(a) compared with different static dewetting thresholds,  $V_U$  (5.4) and  $V_P$  (5.5). From filled circles to open diamonds:  $h_{VE} = 0.4, 0.3, 0.267, 0.24, 0.2$  and  $0.15$ . (a) Compared with critical volume for the existence of unduloids:  $V_U = 1.73\pi R^3$  (5.4); (b) compared with critical volume for the existence of fully wetting spherical liquid plugs:  $V_P = \pi R^3(\Lambda - 4/3)$  (5.5); (c,d) Bond numbers for liquid unduloids,  $Bo_U = \rho_1 g h_{VE}^2 / \sigma$ , and liquid plugs,  $Bo_P = Bo = \rho_1 g R^2 / \sigma$ .

We proceed with figures 14 and 15, where we discuss the effect of different control parameters that are important in the treatment of diseases involving airway occlusion, i.e.  $Re_{20}$ , which is representative of the tracheal breathing flow rate imposed during assisted ventilation, and the Kapitza number,  $Ka$ , Laplace number,  $La = R^* \sigma \rho_1 / \mu_1^2$ , and capillary number,  $Ca = \mathcal{U}_2 \mu_1 / \sigma$ , which characterize the hydrodynamic physical properties of mucus and can typically be modified via medication, e.g. via mucolytics (acting on the mucus viscosity) or surfactants (acting on the surface tension). We consider the same reference parameters as in figure 10, focusing on one liquid holdup,  $h_{VE} = 0.24$ , and we vary  $Re_{20}$  (figure 14a,b),  $Ka$  (figure 14c,d),  $La$  (figure 15a,b) and  $Ca$  (figure 15c,d) around their reference values (marked by thin vertical lines in figure 14 and open circles in figure 15).

Figure 14(a,b) represent the minimum core radius of TSS vs  $Re_{20}$  for  $h_{VE} = 0.24$ . The curve parameter is the airway generation  $n$ , which we have varied from  $n = 10$  (filled circles) to  $n = 14$  (asterisks), and, as in figure 10, we track the linearly most-dangerous TSS by fixing  $k = k_{max}$ . The considered range of  $Re_{20}$  is limited by the turbulence threshold,  $|Re_{20}| \sim 1300$ . Based on the curves in figure 14(a,b), we observe that TPS can be effectively prevented by increasing  $|Re_{20}|$  beyond a threshold that increases with increasing  $n$ . Further, for the proximal airways (closer to the trachea, e.g. pentagons,

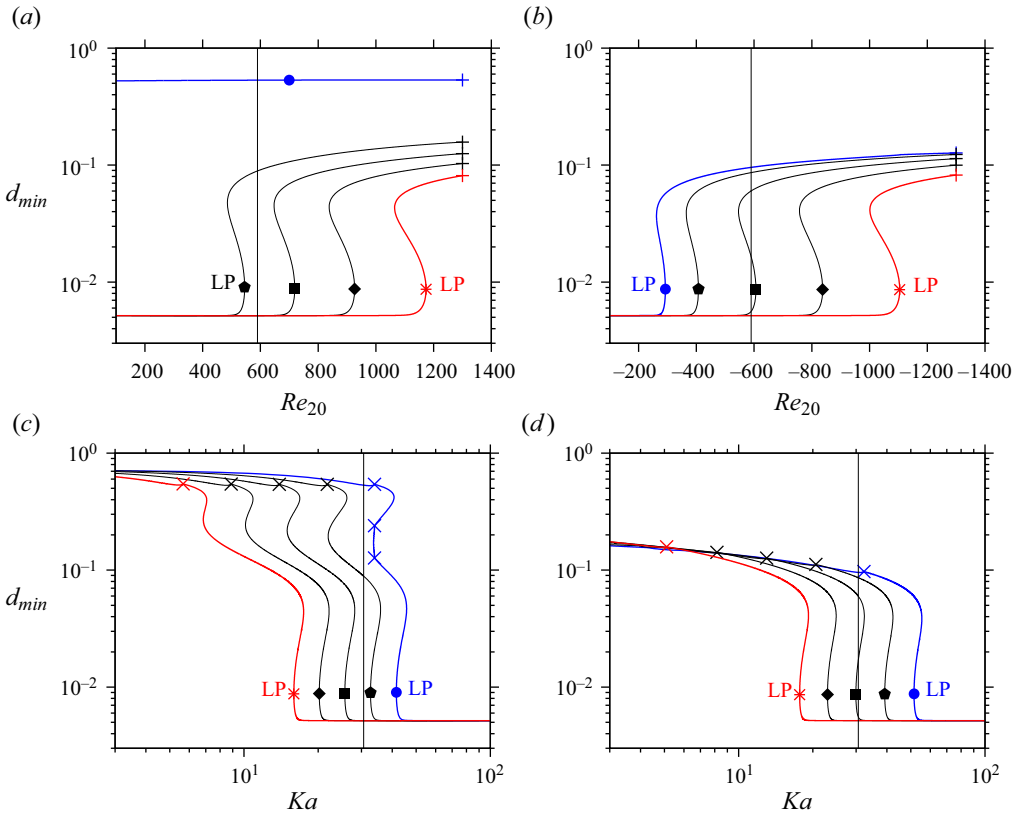


Figure 14. Effect of air flow and mucus properties on airway occlusion. The TSS for reference parameters from figure 10:  $k = k_{max}$ ,  $R^* = R_{Weib}^*$ ,  $Re_2 = Re_2^{Weib}$ ,  $h_{VE}/R = 0.24$ , air I in table 1. Circles:  $n = 10$ , pentagons:  $n = 11$ , squares:  $n = 12$ , diamonds:  $n = 13$  asterisks:  $n = 14$ . Reference state (thin vertical lines):  $Ka = 30.6$ ,  $Re_{20} = \pm 590$ . (a) Versus  $Re_{20}$ , co-current; (b) vs  $Re_{20}$ , counter-current; (c) vs  $Ka$  at fixed  $Ga = R^{*3}g/v_1^2$ ;  $Re_{20} = 590$ ; (d) vs  $Ka$  at fixed  $Ga$ :  $Re_{20} = -590$ . Pluses in panels (a,b) mark turbulence onset.

corresponding to  $n = 11$ ), we observe a non-negligible difference between the co-current (figure 14a,  $Re_{20} > 0$ ) and counter-current (figure 14b,  $Re_{20} < 0$ ) configurations. Once again, we point out that  $Re_{20}$  varies in time over the course of a real breathing cycle. Thus, even if the mean  $|Re_{20}|$  lies beyond the TPS bound given in figure 14(a,b), there is still a risk of airway occlusion in between the inspiration and expiration strokes. In an effective assisted ventilation protocol, this can be avoided by applying a step-like variation of the air flow rate, with a rapid change from inspiration to expiration (Weber *et al.* 2020). Finally, as can be deduced from the absence of crosses in figure 14(a,b), the nature of the instability remains unchanged during a variation of  $Re_{20}$ , i.e. CI for  $n = 10$  and AI for  $n > 10$ .

We now turn to figure 14(c,d), where we have plotted  $d_{min}$  vs  $Ka$  for TSS at  $Re_{20} \pm 590$ ,  $k = k_{max}$  and  $n$  fixed according to figure 14(a,b). Further, we have fixed the liquid Galileo number,  $Ga = R^{*3}g/v_1^2$ , and thus our variation of  $Ka$  mimics a change in mucus surface tension at fixed dynamic viscosity, i.e. via surfactants. Based on these results, we may conclude that the formation of TPS can be prevented by reducing  $Ka$ , e.g. by reducing surface tension. In particular, at the considered  $h_{VE} = 0.24$ , airway occlusion can be avoided for  $n \leq 14$  via reducing  $Ka$  by a factor of roughly 3 vs its reference value (marked by thin vertical lines). And, comparing figures 14(c) and 14(d), we observe that

## Liquid plugs in narrow tubes

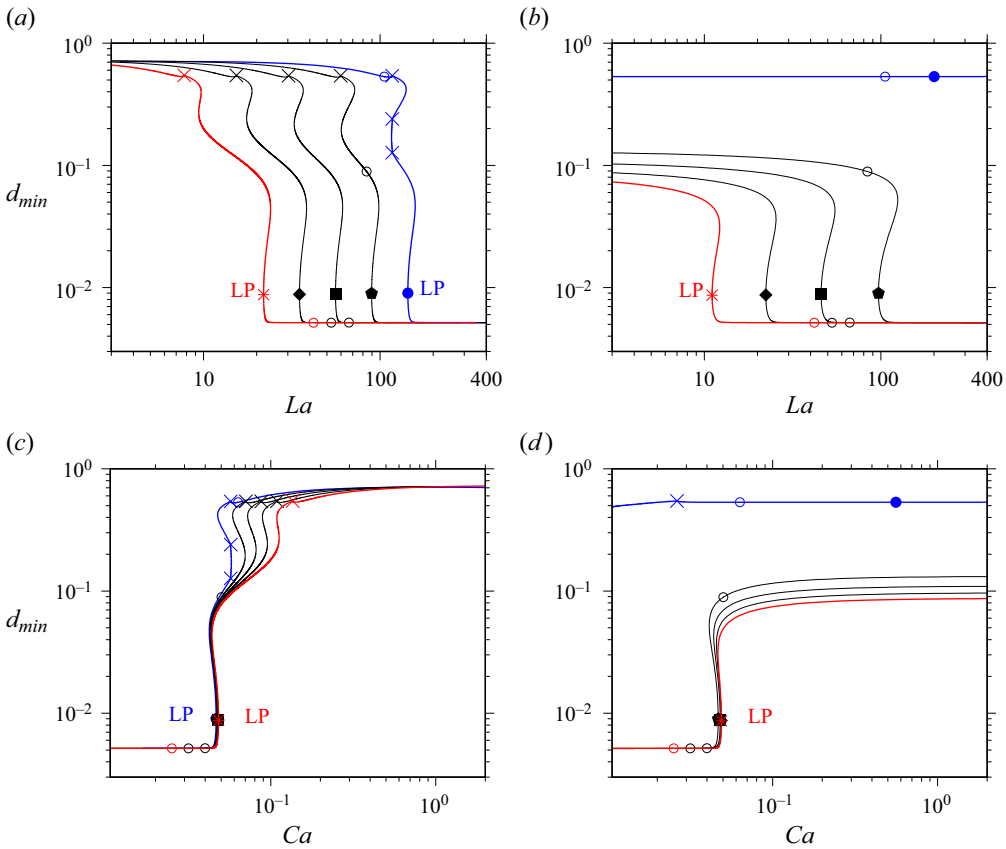


Figure 15. Effect of mucus surface tension and viscosity on airway occlusion. The TSS for reference parameters of co-current configuration in figure 10: air I in table 1,  $k = k_{max}$ ,  $R^* = R_{Weib}^*$ ,  $Re_2 = Re_2^{Weib}$ ,  $R_0^* = 9$  mm,  $Q_{20}^* = 2.5 \times 10^{-4}$  m<sup>3</sup> s<sup>-1</sup>,  $h_{VE}/R = 0.24$ . Circles:  $n = 10$ , pentagons:  $n = 11$ , squares:  $n = 12$ , diamonds:  $n = 13$ , asterisks:  $n = 14$ . (a) Change in  $La = R^* \sigma \rho_1 / \mu_1^2$  at fixed  $Ga = R^{*3} g / v_1^2$ ; (b) change in  $La$  at fixed  $Bo = \rho_1 g R^{*2} / \sigma$ ; (c) data from panel (a) vs  $Ca = \mathcal{U}_2 \mu_1 / \sigma$ ; (d) data from panel (b) vs  $Ca$ . Absolute instability everywhere except on branch to the right of blue cross. In all panels, open circles correspond to  $Ka = 30.6$ , i.e. mucus I in table 1.

slightly lower values of  $Ka$  are required to avoid occlusion in the co-current (figure 14c) vs the counter-current (figure 14d) configuration. Finally, we observe that increasing  $Ka$  causes a transition from CI to AI, and that all plotted TPS branches lie entirely in the AI regime.

In figure 15(a,c), we have re-plotted the TSS from figure 14(c), which corresponds to the co-current configuration, in terms of  $La$  and  $Ca$ . We recall that  $Ga$  is fixed in these calculations, so that they mimic a change in mucus surface tension at constant mucus dynamic viscosity, i.e. via surfactants. Interestingly, the onset of TPS in figure 15(c) collapses to a single threshold for all considered airway generations, i.e.  $Ca \sim 0.05$ .

By contrast, figure 15(b,d) represents TSS obtained by varying  $La$  and  $Ca$  at constant Bond number,  $Bo = \rho_1 g R^{*2} / \sigma$ . This mimics a change in mucus dynamic viscosity at constant mucus surface tension, e.g. via mucolytics. Based on these results, we may conclude that an increase in mucus viscosity allows us to suppress TPS in favour of TWS. However, the resulting TWS are associated with small values of the core radius  $d_{min}$ . Thus, although liquid plugs can be suppressed by increasing mucus viscosity, the

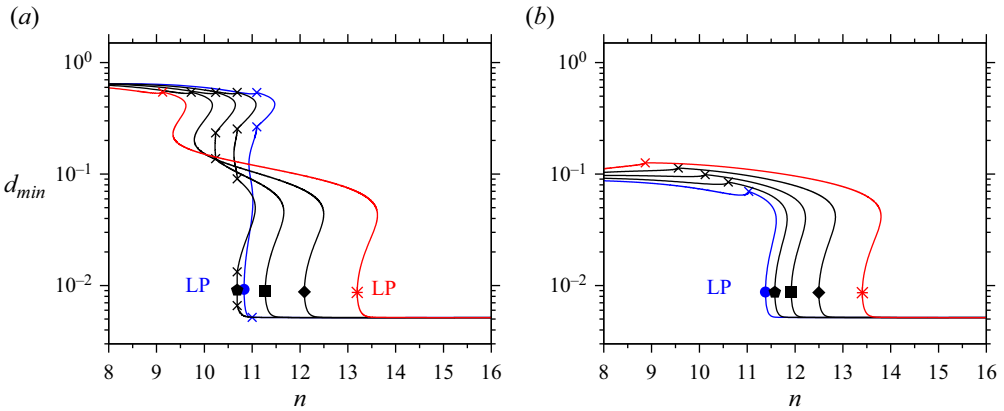


Figure 16. Self-similar airway contraction/expansion based on lung architecture model (5.1) of Weibel & Gomez (1962). Effect of  $R_0^*$  on TSS:  $k = k_{max}$ ,  $R^* = R_{Weib}^*$ ,  $Re_2 = Re_2^{Weib}$ ,  $Ka = 30.6$  (mucus I and air I in table 1),  $h_{VE} = 0.24$ . Circles:  $R_0^* = 11$  mm, pentagons:  $R_0^* = 10$  mm, squares:  $R_0^* = 9$  mm, diamonds:  $R_0^* = 8$  mm, asterisks:  $R_0^* = 7$  mm. (a) Co-current configuration:  $M_{dry} < 0$ ,  $Q_{20}^* = 2.5 \times 10^{-4} \text{ m}^3 \text{ s}^{-1}$ ; (b) counter-current configuration:  $M_{dry} > 0$ ,  $Q_{20}^* = -2.5 \times 10^{-4} \text{ m}^3 \text{ s}^{-1}$ .

airways nonetheless remain significantly obstructed, except for  $n = 10$  (blue curves with filled circles), where non-occluding TWS exist over the entire  $La$  and  $Ca$  ranges. This is in contrast to suppressing liquid plugs via surfactants (figure 15a,c).

Over the course of a breathing cycle, the lung expands during inspiration and contracts during expiration (Grotberg 1994), according to a tidal volume of  $V_T \sim 500 \times 10^{-6} \text{ m}^3$  in the case of an adult (Halpern *et al.* 1998). Also, the lung geometry can differ quantitatively from one individual to another. Such geometrical effects are bound to modify the threshold for airway occlusion. We investigate this in a rudimentary way by changing the trachea radius  $R_0^*$ , while keeping the gas flow rate  $Q_{20}^* = 2.5 \times 10^{-4} \text{ m}^3 \text{ s}^{-1}$  constant. This amounts to assuming a self-similar contraction/expansion of the lung architecture, as controlled by  $R_0^*$  via (5.1).

Figure 16 represents TSS, in the form of  $d_{min}$  vs  $n$  curves, as obtained for different values of  $R_0^*$ , ranging from  $R_0^* = 7$  to  $R_0^* = 11$  mm, for the co-current (figure 16a) and counter-current (figure 16b) configurations. In both configurations, the onset of TPS is delayed toward distal airways upon decreasing  $R_0^*$  (compare curves with circles with curves with asterisks). This is because  $Re_{20}$  increases with decreasing  $R_0^*$  at constant  $Q_{20}^*$ , and we have seen in figure 14(a,b) that increasing the strength of the air flow delays airway occlusion. Comparing figures 16(a) and 16(b), we observe that the effect of  $R_0^*$  is approximately the same for the co-current and counter-current configurations. Finally, we observe that the CI/AI transition moves to more distal airways as  $R_0^*$  is reduced, and that almost all TPS lie in the AI regime.

### 5.2. Wall stresses based on TSS

In § 4, we have shown that our WRIBL model (2.13) can accurately predict the wall stresses developed within the liquid film of a TPS, as well as the axial spatial derivatives of these stresses (see figure 7). Several studies have provided clear evidence that these mechanical quantities are responsible for damaging epithelial cells within the pulmonary airways, as a result of liquid plugs formed by the mucus film lining their inner surface. These studies either focused on a particular airway generation (Muradoglu *et al.* 2019), or simplified



the problem with respect to the pulmonary setting, e.g. by using rectangular instead of cylindrical channels (Bilek *et al.* 2003; Fujioka & Grotberg 2004; Kay *et al.* 2004; Huh *et al.* 2007; Zheng *et al.* 2007), or by neglecting gravity (Fujioka *et al.* 2008; Hassan *et al.* 2011; Olgac & Muradoglu 2013; Fujioka *et al.* 2016) or advection via the gas flow (Romano *et al.* 2021). Several of these works aimed at establishing correlations based on the fluid mechanical control parameters. In the current section, we aim to complement these works by accounting for how these parameters evolve throughout the respiratory network.

For this, we use our TSS from § 5.1 to investigate how the maximum magnitudes of the mechanical wall stresses and their space and time derivatives (calculated according to (4.1) and (4.2) § 4), evolve throughout the respiratory network, and how they are affected by the main control parameters. By comparing our WRIBL predictions of these measures with the *ex vivo* experimental data of Bilek *et al.* (2003) and Kay *et al.* (2004), we can assess the damage potential for epithelial cells.

In figure 17, we plot the maximum magnitudes of the wall shear stress (figure 17a),  $\tau_w$  (4.2b) and excess pressure (figure 17b),  $\Delta p_w$  (4.1), vs the airway generation,  $n$ , for the TSS in figure 10(a), where crosses mark the CI/AI transition and other symbols mark LPs corresponding to the onset of TPS (superscripts max and min will refer to extrema across the spatial profile of a TSS throughout). These maximum magnitudes are associated with the capillary ripple preceding the leading front of the liquid plug (Fujioka & Grotberg 2004; Zheng *et al.* 2007), which can be seen in figure 7(a). From figure 17(a), we may conclude that the maximum wall shear stress magnitude,  $|\tau_w^*|^{max}$ , associated with TPS (curve portions to the right of polygonal symbols except for open diamonds) is an order of magnitude larger than in the *ex vivo* experiments of Kay *et al.* (2004), i.e.  $|\tau_w^*|^{max} \sim 10$  Pa here vs  $|\tau_w^*|^{max} \sim 1$  Pa in the experiments, where significant epithelial cell damage was observed.

The trend of the  $|\tau_w^*|^{max}$  vs  $n$  curves in figure 17(a) is not trivial. Although the transition from TWS to TPS is always associated with a significant increase in the stress magnitude,  $|\tau_w^*|^{max}$ , the latter quantity can intermediately decrease with increasing  $n$  for TPS (see e.g. curves with filled circle and filled pentagon). As a result, the overall maximum of  $|\tau_w^*|^{max}$  is not necessarily associated with the most distal airways. We also point out that, for  $n \geq 14$ , the stress magnitude is dictated by the stress minimum,  $\tau_w^{*min}$ , as can be deduced by comparing figures 17(c) and 17(d), which represent  $\tau_w^{*min}$  and the stress maximum,  $\tau_w^{*max}$ , with figure 17(a). The excess pressure,  $|\Delta p_w^*|^{max}$ , represented in figure 17(b), displays more or less the same behaviour as  $|\tau_w^*|^{max}$ , only that it attains considerably larger magnitudes in the most distal airways.

We now turn to figure 18, which represents the spatial and temporal derivatives of the wall shear stress,  $\tau_w$  (figure 18a,c), and of the wall pressure,  $p_w$  (figure 18b,d) in terms of the airway generation,  $n$ , for the TSS in figure 10(a). The seminal experiments of Kay *et al.* (2004) have proven that the maximum magnitude of the axial wall pressure derivative within a liquid plug,  $|\partial_{x^*} p_w^*|^{max}$  (figure 18b), is directly correlated with epithelial cell damage. According to our figure 18(b), TSS attain the required level for high cell damage according to table 1 in Kay *et al.* (2004), i.e.  $|\partial_{x^*} p_w^*|^{max} \sim 0.6 \text{ Pa } \mu\text{m}^{-1}$ , for all values of  $h_{VE}$ , i.e. in the most distal airways ( $n \geq 14$ ). Further, the level for low but appreciable cell damage,  $|\partial_{x^*} p_w^*|^{max} \sim 0.3 \text{ Pa } \mu\text{m}^{-1}$ , can be attained in quite proximal airways, i.e.  $n = 6$  for  $h_{VE} = 0.4$  (blue line with filled circle).

According to figure 18(a), the maximum magnitude of the wall shear stress derivative,  $|\partial_{x^*} \tau_w^*|^{max}$ , is comparable in magnitude and behaves similarly to that of the wall pressure derivative in figure 18(b). This is a significant difference with the experiments of Kay *et al.* (2004), where the wall shear stress derivative was an order of magnitude smaller.

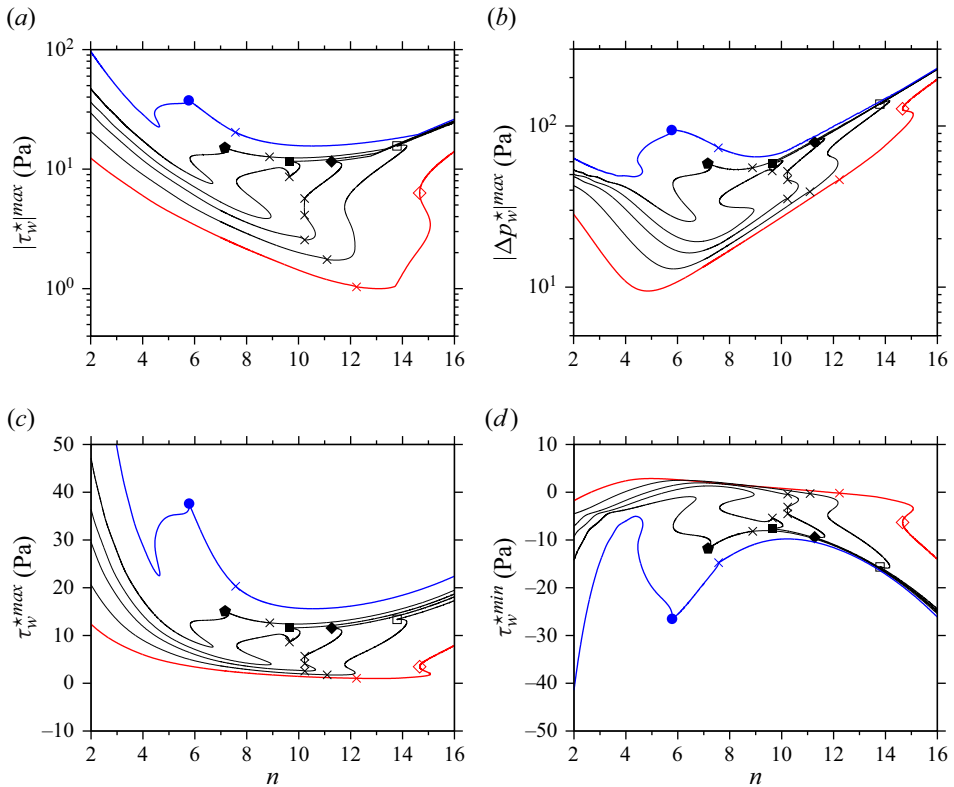


Figure 17. Wall stresses for TSS in figure 10(a). Co-current configuration:  $Re_{20} = 590$ ,  $Ka = 30.6$ ,  $k = k_{max}$ ,  $R^* = R_{Weib}^*$ ,  $Re_2 = Re_2^{Weib}$ . Crosses mark CI/AI transition and other symbols correspond to LPs in figure 10(a), marking the onset of TPS (except for open diamonds). Filled circles to asterisks:  $h_{VE} = 0.4, 0.3, 0.267, 0.24, 0.2$ , and  $0.15$ . (a) Maximum magnitude of wall shear stress,  $\tau_w$  (4.2b); (b) maximum magnitude of excess pressure,  $\Delta p_w$  (4.1); (c,d) maximum and minimum values of  $\tau_w$ .

This discrepancy could be due to the different flow configuration used in the experiment, i.e. a rectangular horizontal channel instead of a cylindrical tube. By contrast, our results in figure 18(a) imply that the spatial wall shear stress derivative is sufficiently large to cause significant epithelial cell damage. Moreover, as the loci of  $|\partial_x \tau_w^*|^{max}$  and  $|\partial_x p_w^*|^{max}$  do not coincide, but lie close to one another in the region of the capillary ripple downstream of the leading plug front (see figure 7c,d), the passage of a TPS subjects the epithelial cells to a double mechanical solicitation of lethal magnitude.

In that context, it is useful to evaluate the maximum magnitudes of the temporal derivatives of the wall stresses,  $|\partial_t \tau_w^*|^{max}$  and  $|\partial_t p_w^*|^{max}$ , which are represented in figure 18(c,d). For TSS, these quantities can be obtained from the spatial derivatives via the transformation  $\partial_t = -c \partial_x$ , where  $c$  denotes the TSS propagation speed. We observe that the overall maxima of  $|\partial_t \tau_w^*|^{max}$  and  $|\partial_t p_w^*|^{max}$  across the considered airway generation range can occur at significantly more proximal airways vs the spatial derivatives represented in figure 18(a,b). For example, at  $h_{VE} = 0.4$  (curves with filled circles), the overall maximum of  $|\partial_t \tau_w^*|^{max}$  for TPS is reached at  $n = 6$  (figure 18c), whereas the overall maximum of  $|\partial_x \tau_w^*|^{max}$  is reached at  $n = 16$  (figure 18a). Thus, the question arises as to whether epithelial cell damage is mainly driven by the temporal or the spatial variation of wall stresses.

## Liquid plugs in narrow tubes

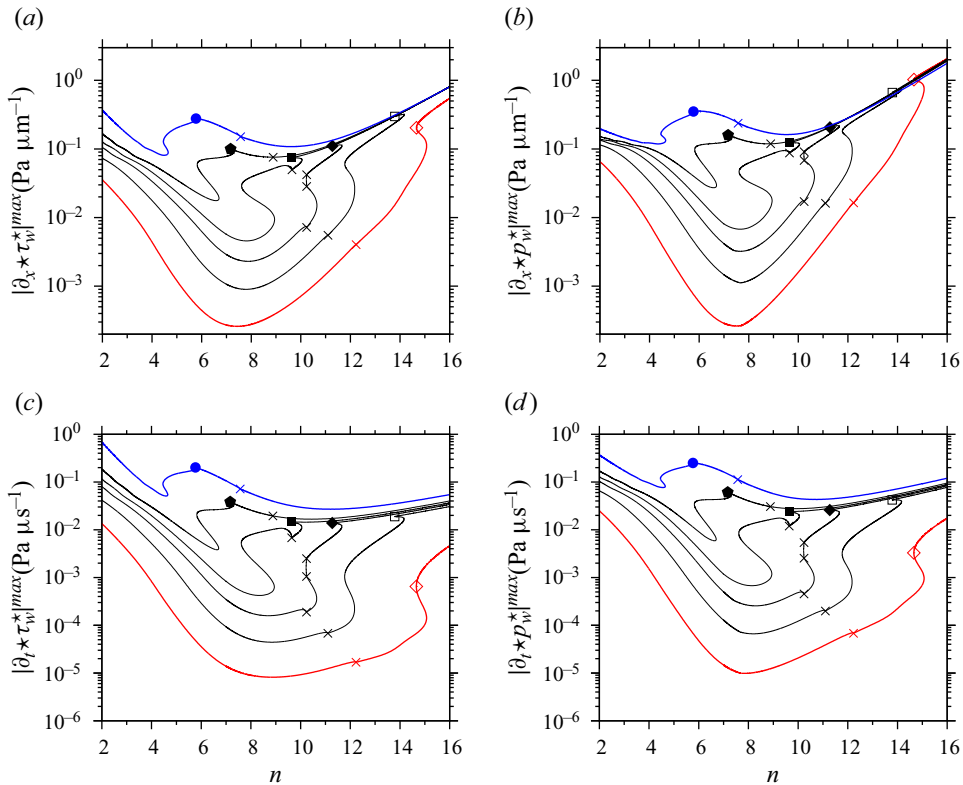


Figure 18. Maximum magnitudes of wall stress derivatives for TSS in figure 10(a). Same parameters and attributions as in figure 17. (a,c) Wall shear stress  $\tau_w$  according to (4.2b); (b,d) wall pressure  $p_w$  according to (4.2a); (a,b) spatial derivative  $\partial_x$ ; (c,d) temporal derivative  $\partial_t = -c\partial_x$ .

Figure 19 represents the maximum magnitudes of the spatial wall stress derivatives for the counter-current configuration, i.e. for the TSS in figure 10(b). In that case, TWS are associated with much smaller values of  $d_{min}$  and this greatly affects the wall stress derivatives. In particular, the overall maximum of  $|\partial_x \tau_w^*|^{max}$  is reached in the most proximal airways for almost all values of  $h_{VE}$  (figure 19a), and lies well above the threshold for significant epithelial cell damage ( $|\partial_x \tau_w^*| \sim 1 \text{ Pa } \mu\text{m}^{-1}$ ), whereas it is always reached in the most distal airways for the co-current configuration (figure 18a). Also, the overall minimum of  $|\partial_x \tau_w^*|^{max}$  for the counter-current configuration (figure 19a) is greater by one order of magnitude vs the co-current configuration (figure 18a), meaning that the average level of mechanical solicitation is much greater in the counter-current configuration. Similar observations can be made for  $|\partial_x p_w^*|^{max}$  in figure 19(b) vs figure 18(b). Thus, the orientation of a particular airway with respect to gravity may have a significant effect on the level of epithelial cell damage.

We proceed with figure 20, which reports the effects of the tracheal Reynolds number,  $Re_{20}$ , the Kapitza number,  $Ka$ , and the tracheal airway radius,  $R_0^*$ , on the maximum magnitude of the spatial derivative of the tangential wall shear stress,  $|\partial_x \tau_w^*|^{max}$ . According to figure 20(a,b), which corresponds to the TSS for the co-current and counter-current configurations in figure 14(a,b), the effect of  $Re_{20}$  is rather weak for all considered airway generations (from filled blue circles, marking  $n = 10$ , to red asterisks, marking  $n = 14$ ). Thus, avoiding airway occlusion by increasing  $|Re_{20}|$ , as discussed with

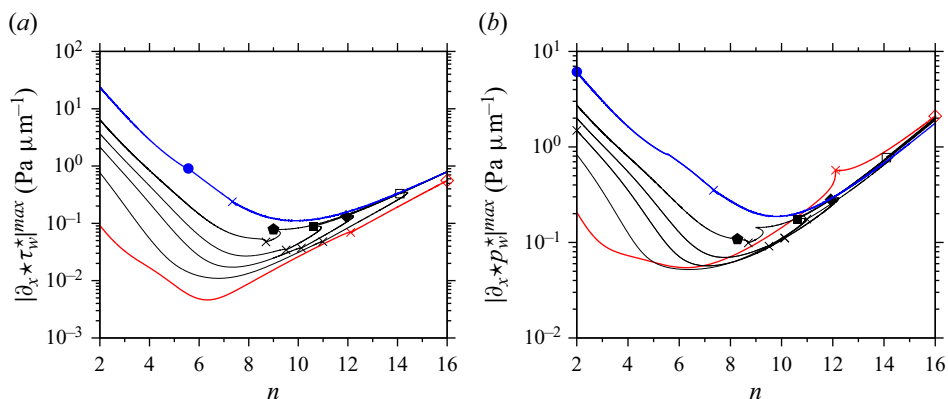


Figure 19. Maximum magnitudes of spatial wall stress derivatives for TSS in figure 10(b). Counter-current configuration:  $Re_{20} = -590$ ,  $Ka = 30.6$ ,  $k = k_{max}$ ,  $R^* = R_{Weib}^*$ ,  $Re_2 = Re_2^{Weib}$ . Crosses mark CI/AI transition and other symbols correspond to LPs in figure 10(a), marking the onset of TPS (except for open diamonds). Filled circles to asterisks:  $h_{VE} = 0.4, 0.3, 0.267, 0.24, 0.2$  and  $0.15$ . (a) Derivative of wall shear stress,  $\tau_w^*$ , according to (4.2b); (b) derivative of wall pressure,  $p_w$ , according to (4.2a).

respect to figure 14(a,b), comes at the expense of producing an additional wall shear stress, so that epithelial cell damage cannot be reduced in the end.

By contrast, figure 20(c), which reports the effect of the Kapitza number based on the TSS in the counter-current configuration of figure 14(c), shows that avoiding TPS by reducing  $Ka$  at constant  $Ga$  is associated with a very significant reduction in  $|\partial_{x^*} \tau_w^*|^{max}$ , i.e. by one order of magnitude. Also, on the TPS branches (curve portions to the right of the symbols marking LPs in figure 20c),  $|\partial_{x^*} \tau_w^*|^{max}$  diminishes with decreasing  $Ka$  according to a power law, i.e.  $|\partial_{x^*} \tau_w^*|^{max} \propto Ka^C$ , where  $C > 0$  is a constant. Thus, decreasing  $Ka$ , i.e. by reducing the mucus surface tension, may help to significantly reduce the level of epithelial cell damage. We point out that we have compared our TPS data from figure 20(c) with the correlation in equation (33) of Fujioka *et al.* (2016) by re-plotting these in terms of the modified capillary number,  $\overline{Ca} = \mu_1 c^* / \sigma$ , and evaluating the minimum film thickness,  $h_{min}$ . Although the trend of  $|\partial_{x^*} \tau_w^*|^{max}$  vs  $\overline{Ca}$  is similar, the trend in terms of the airway generation,  $n$ , is inverted. This may be due to the finite length of the TPS considered here (infinite plugs were considered in the reference), or the effect of inertia and/or axial viscous diffusion, which were not accounted for in the model of Fujioka *et al.* (2016).

Finally, figure 20(d) demonstrates the effect of a self-similar expansion/compression of the lung, by plotting  $|\partial_{x^*} \tau_w^*|^{max}$  vs  $n$  for the TSS in figure 16(a), which corresponds to different values of the tracheal airway radius,  $R_0^*$ . Even though a reduction of  $R_0^*$  allows us to delay the formation of TPS to more distal airways (as discussed with respect to figure 16a), its net effect is to increase the wall stress derivative for all  $n$ . This is due to the fact that the tracheal gas flow rate,  $Q_0^*$ , is kept constant in figure 20(d), which means that  $Re_2$  increases at a given  $n$  when decreasing  $R_0^*$ .

## 6. Conclusion

In the current manuscript, we have used the augmented cylindrical WRIBL model (2.13), which was proposed in the appendix of Dietze *et al.* (2020), to simulate liquid plugs in narrow cylindrical tubes. In the first part (§ 4), we have extensively validated our model by comparing with occlusion experiments from the literature and with our own DNS.

## Liquid plugs in narrow tubes

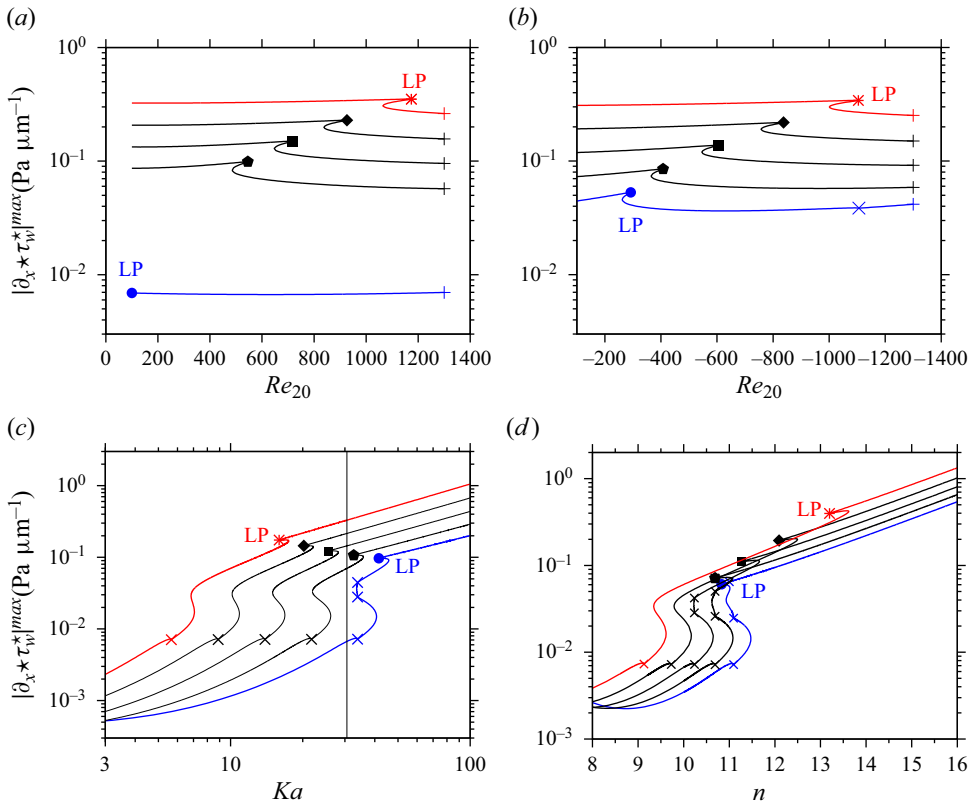


Figure 20. Effect of different control parameters on the maximum magnitude of the spatial wall shear stress derivative,  $\partial_x \tau_w$  (4.2b). Parameters and symbols as in figures representing corresponding TSS. (a) Effect of air flow: co-current configuration. The TSS according to figure 14(a); (b) effect of air flow: counter-current configuration. The TSS according to figure 14(b); (c) change in  $Ka$  at fixed  $Ga$ : co-current. The TSS according to figure 14(c); (d) effect of trachea radius  $R_0^*$ : co-current. The TSS according to figure 16(a).

Thereby, we have demonstrated that our model accurately captures: (i) the linear and nonlinear dynamics of liquid plug formation (figures 4 and 8); (ii) the flow field associated with TPS (figure 6); (iii) the speed and entrained gas flow rate of TPS and their variation with the liquid volume (figures 5 and 9); and (iv) the associated tangential and normal wall stresses, as well as their spatial derivatives (figure 7). In the second part (§ 5), we then applied our WRIBL model to predict liquid-plug formation by the mucus film coating the inner surface of the pulmonary airways, based on a continuum representation of the tracheobronchial tree, using the lung architecture model (5.1) of Weibel & Gomez (1962), which describes how the airway radius,  $R^*$ , air Reynolds number,  $Re_2$ , and airway length,  $L^*$ , vary with the airway generation,  $n$ . Here, we have assumed typical conditions for assisted ventilation (Halpern *et al.* 1998), and taken into account the effect of gravity by comparing the co-current and counter-current configurations.

This was done via low-cost calculations based on numerical continuation that allow us to track the evolution of TSS, i.e. TWS and TPS, in terms of  $n$ , throughout the conductive region of the tracheobronchial tree ( $n < 16$ ). An important feature of our WRIBL model is that it provides a direct continuation path from TWS to TPS (see e.g. figure 3), which allows us to readily identify the threshold for liquid-plug formation, e.g.

in terms of the airway generation,  $n$  (see e.g. [figure 10](#)). In our continuation calculations, we have imposed the most-dangerous wave number,  $k = k_{max}$ , which is either given by the spatially most-amplified mode, in the case of CI, or by the absolute mode, in the case of AI. This wavenumber,  $k_{max}$ , is determined via simultaneous (spatial or spatio-temporal) linear stability calculations based on the dispersion relation of our WRIBL model (3.3), which allow us to identify the CI/AI transition (Brevdo *et al.* 1999). As a result, we were able to track TSS that are most likely to emerge in a real system. On the one hand, our WRIBL continuation calculations enabled us to identify the critical conditions for liquid-plug formation in the conducting zone of the tracheobronchial tree, and the effect of the principal control parameters thereon (§ 5.1). On the other hand, they allowed us to predict the maximum magnitude of the wall stresses (and their spatial and temporal derivatives) exerted by the mucus film on the airway wall and to compare these with the thresholds for epithelial cell damage (§ 5.2), as identified in the seminal experiments of Kay *et al.* (2004).

Our main conclusions are as follows. (i) Liquid plugs form for values of the liquid hold up,  $h_{VE}$ , larger than  $h_{VE} \sim 0.15$ , starting in the most distal airways ( $n = 16$ ), and moving toward more proximal airways with increasing  $h_{VE}$ . At  $n = 6$ , a holdup of  $h_{VE} = 0.4$  would be required to reach occlusion, which is quite unlikely in a physiological setting. These observations are in agreement with postmortem studies identifying the major sites of airway obstruction in chronic obstructive pulmonary disease at  $n \geq 8$  (Corrin & Nicholson 2011) and with the state of the art on this topic published by Hogg (2006). (ii) The TPS are associated with a very significant increase in the pressure drop when the gas flow rate,  $Q_2^*$ , is imposed ([figure 10c](#)), and with a drastic reduction in  $Q_2^*$  when the gas pressure drop is imposed ([figure 11b](#)). (iii) In most cases, TPS lie in the AI regime, i.e. the base flow is absolutely unstable and plug formation is highly likely. (iv) Although the critical  $n$  for TPS formation is not significantly affected by the airway orientation with respect to gravity, TWS in the counter-current case display a much larger amplitude (compare [figures 10a](#) and [10b](#)), which leads to a significant increase (by more than one order of magnitude) of the gas pressure drop (compare [10c](#) and [10d](#)). (v) In some regimes, the liquid volume associated with TWS and TPS can lie below the limit for liquid unduloids or fully wetting spherical liquid plugs ([figure 13a,b](#)), making a dewetting of the mucus film possible, e.g. in between inspiration and expiration strokes. (vi) While the typical wavelength of TPS corresponds to approximately half the length of a considered airway,  $\Lambda/L_{Weibel} \sim 0.5$ , their travelling distance is many times larger than  $L_{Weibel}$  ([figure 12](#)), meaning that liquid plugs can easily propagate into more distal airways. (vii) Liquid-plug formation can be avoided in all generations by increasing the air flow rate ([figure 14a,b](#)), e.g. via assisted ventilation, and by reducing the surface tension via surfactants (variation of Kapitza number at constant liquid Galileo number in [figure 14c,d](#)). Although TPS can also be suppressed by increasing mucus viscosity (reduction of Laplace number at constant Bond number in [figure 15b](#)), the resulting TWS still significantly obstruct the airways. For a given liquid holdup, the onsets of TPS in distal airway generations collapse to a single critical value for the capillary number,  $Ca$  ([figure 15c,d](#)). (viii) Contraction/expansion of the lung, moves the critical airway generation for TPS formation to more distal/proximal airways ([figure 16](#)). (ix) Transition from TWS to TPS is associated with a drastic increase in the maximum magnitudes,  $|\partial_{x^*} \tau_w^*|^{max}$  and  $|\partial_{x^*} p_w^*|^{max}$ , of the spatial derivatives of the tangential and normal wall stresses ([figure 18](#)), and both magnitudes attain values well beyond the limit for epithelial cell damage according to the *ex vivo* experiments of Kay *et al.* (2004), even in quite proximal airways ( $n = 6$ ). (x) Depending on the orientation of gravity, the wall stress derivative magnitudes attain their maxima in the most proximal

(counter-current configuration, [figure 19a](#)) or in the most distal (co-current configuration, [figure 18a](#)) airways. (xi) The temporal wall stress derivative magnitudes,  $|\partial_{t^*} \tau_w^*|^{max}$  and  $|\partial_{t^*} p_w^*|^{max}$ , attain their maximum in much more proximal airways vs the spatial derivatives ([figure 18c,d](#)). Thus, determining which one of these measures is most representative to assess epithelial cell damage is an important future task. (xii) Preventing TPS formation by increasing the air flow rate ([figure 14a,b](#)) is associated with consistently high levels of the spatial wall shear stress derivative ([figure 20a,b](#)). In some cases, these lie beyond the threshold for epithelial cell damage. (xiii) A significant reduction in the wall stress derivatives can be achieved by reducing mucus surface tension ([figure 20c](#)).

Future work should focus on extending our WRIBL model to further approach the physiological setting of airway occlusion. In particular, the model should be extended to the fully three-dimensional case, in order to represent configurations where the airway is not aligned with gravity (Suresh & Grotberg 2005). Another promising direction is to study plug formation via transient computations (Fujioka *et al.* 2016; Romano *et al.* 2021). This would allow us to simulate assisted ventilation regimes with the goal of predicting optimal operating conditions, where plug formation is avoided over the course of a breathing cycle while wall stresses (and the associated epithelial cell damage) are minimized. Also, the presence of the PCL layer (Ogrosky 2021a), the effect of beating cilia (Bottier *et al.* 2017), the non-Newtonian mucus rheology (Vasquez *et al.* 2016) and the secretion of mucus should be accounted for. On the other hand, our model could be applied to other configurations involving liquid plugs, e.g. for the cleaning of contaminated surfaces (Zoueshtiagh *et al.* 2014; Khodaparast *et al.* 2017) or the filtering of particles (Yu, Khodaparast & Stone 2018). In the context of SRT, it would be interesting to study the stability of the TPS predicted by our WRIBL model. Instability can represent a second route toward plug rupture, which may occur earlier than the loss of TPS at the LP connecting TWS and TPS (LP2 in [figure 3a](#)). Such an investigation would allow us to extend the work of Ubal *et al.* (2008), where gravity was neglected.

**Acknowledgements.** The author wishes to thank C. Ruyer-Quil and M. Filoche for fruitful discussions.

**Funding.** The author gratefully acknowledges funding provided by CNRS Ingénierie via équipe-project MUCUS.

**Declaration of interests.** The author reports no conflict of interest.

**Author ORCIDs.**

 Georg F. Dietze <https://orcid.org/0000-0003-1495-5505>.

## Appendix A. Full expressions for coefficients introduced in § 2

The source terms,  $Z_k$ , in the boundary value problem (2.9) for the axial base velocity profiles,  $\hat{u}_k$ , are defined as follows:

$$Z_1 = -Re_1^{-1} \{C_{11}Q_1 + C_{12}Q_2\}, \quad Z_2 = -Re_2^{-1} \{C_{21}Q_1 + C_{22}Q_2\}, \quad (A1a)$$

with the constants,  $C_{ij}$ , according to:

$$C_{11} = \frac{8}{E} \{4\Pi_\mu [\ln(d) - \ln(R)] - 1\}, \quad (A1b)$$

$$C_{12} = \frac{16}{\mathcal{E}} \frac{\Pi_\mu \Pi_u}{d^2} \{2d^2 [\ln(d) - \ln(R)] - d^2 + R^2\}, \quad (\text{A1c})$$

$$C_{21} = \frac{16}{\mathcal{E}} \frac{1}{d^2 \Pi_u} \{2d^2 [\ln(d) - \ln(R)] - d^2 + R^2\}, \quad (\text{A1d})$$

$$C_{22} = \frac{8}{\mathcal{E}} \frac{1}{d^4} \{4d^4 [\ln(d) - \ln(R)] - 3d^4 + 4d^2 R^2 - R^4\}, \quad (\text{A1e})$$

where the common term,  $\mathcal{E}$ , is defined as

$$\begin{aligned} \mathcal{E} = \pi \{ & 4[d^4(\Pi_\mu - 1) - \Pi_\mu R^4](\ln(d) - \ln(r)) \\ & - (d^2 - R^2)[d^2(4\Pi_\mu - 3) + (1 - 4\Pi_\mu)R^2] \}, \end{aligned} \quad (\text{A1f})$$

and where the chosen scaling implies  $R = 1$ .

The coefficients,  $f_{ki}$ , of the axial base velocity profiles,  $\hat{u}_k$ , according to (2.10a) are defined as follows:

$$f_{11} = \frac{1}{4} C_{11}(r^2 - R^2) + D_{11} [\ln(r) - \ln(R)], \quad (\text{A2a})$$

$$f_{12} = \frac{1}{4} C_{12}(r^2 - R^2) + D_{12} [\ln(r) - \ln(R)], \quad (\text{A2b})$$

$$f_{21} = \Pi_u^{-1} F_{11} + \frac{1}{4} C_{21}(r^2 - d^2), \quad (\text{A2c})$$

$$f_{22} = \Pi_u^{-1} F_{12} + \frac{1}{4} C_{22}(r^2 - d^2), \quad (\text{A2d})$$

where we have introduced the constants,  $D_{ij}$

$$D_{11} = -\frac{1}{2} d^2 (C_{11} - \Pi_\mu \Pi_u C_{21}), \quad (\text{A2e})$$

$$D_{12} = -\frac{1}{2} d^2 (C_{12} - \Pi_\mu \Pi_u C_{22}). \quad (\text{A2f})$$

#### REFERENCES

- ATASI, O., KHODAPARAST, S., SCHEID, B. & STONE, H.A. 2017 Effect of buoyancy on the motion of long bubbles in horizontal tubes. *Phys. Rev. Fluids* **2**, 094304.
- AUSSILLOUS, P. & QUÉRÉ, D. 2000 Quick deposition of a fluid on the wall of a tube. *Phys. Fluids* **12**, 2367–2371.
- BAHRANI, S.A., HAMIDOUCHE, S., MOAZZEN, M., SECK, K., DUC, C., MURADOGLU, M., GROTBORG, J.B. & ROMANO, F. 2022 Propagation and rupture of elastoviscoplastic liquid plugs in airway reopening model. *J. Non-Newtonian Fluid Mech.* **300**, 104718.
- BAUDOIN, M., SONG, Y., MANNEVILLE, P. & BAROUD, C.N. 2013 Airway reopening through catastrophic events in a hierarchical network. *Proc. Natl Acad. Sci. USA* **110**, 859–864.
- BICO, J. & QUÉRÉ, D. 2001 Falling slugs. *J. Colloid Interface Sci.* **243** (1), 262–264.
- BILEK, A.M., DEE, K.C. & GAVER III, D.P. 2003 Mechanisms of surface-tension-induced epithelial cell damage in a model of pulmonary airway reopening. *J. Appl. Physiol.* **94**, 770–783.
- BOTTIER, M., PEÑA FERNÁNDEZ, M., PELLE, G., ISABEY, D., LOUIS, B., GROTBORG, J.B. & FILOCHE, M. 2017 A new index for characterizing micro-bead motion in a flow induced by ciliary beating. Part II. Modeling. *PLoS Comput. Biol.* **13** (7), e1005552.
- BRETHERTON, F.P. 1961 The motion of long bubbles in tubes. *J. Fluid Mech.* **10**, 166–188.
- BREVDO, L., LAURE, P., DIAS, F. & BRIDGES, T.J. 1999 Linear pulse structure and signalling in a film flow on an inclined plane. *J. Fluid Mech.* **396**, 37–71.



- CAMASSA, R., MARZUOLA, J.L., OGROSKY, H.R. & SWYGERT, S. 2021 On the stability of traveling wave solutions to thin-film and long-wave models for film flows inside a tube. *Physica D* **415**, 132750.
- CAMASSA, R., MARZUOLA, J.L., OGROSKY, H.R. & VAUGHN, N. 2016 Traveling waves for a model of gravity-driven film flows in cylindrical domains. *Physica D* **333**, 254–265.
- CAMASSA, R., OGROSKY, H.R. & OLANDER, J. 2014 Viscous film-flow coating the interior of a vertical tube. Part 1. Gravity-driven flow. *J. Fluid Mech.* **745**, 682–715.
- CAMASSA, R., OGROSKY, H.R. & OLANDER, J. 2017 Viscous film-flow coating the interior of a vertical tube. Part 2. Air-driven flow. *J. Fluid Mech.* **825**, 1056–1090.
- CHANG, H.C., DEMEKHIN, E.A. & KALCIDIN, E. 1996 Simulation of noise-driven wave dynamics on a falling film. *AIChE J.* **42** (6), 1553–1568.
- CHATELIN, R., ANNE-ARCHARD, D., MURRIS-ESPIN, M., THIRIET, M. & PONCET, P. 2017 Numerical and experimental investigation of mucociliary clearance breakdown in cystic fibrosis. *J. Biomech.* **53**, 56–63.
- CHOUDHURY, A., FILOCHE, M., RIBE, N.M., GRENIER, N. & DIETZE, G.F. 2023 On the role of viscoelasticity in mucociliary clearance: a hydrodynamic continuum approach. *J. Fluid Mech.* **971**, A33.
- CORRIN, B. & NICHOLSON, A.G. 2011 *Pathology of the lungs E-book: expert consult: Online and Print*. Elsevier Health Sciences.
- DAO, E.K. & BALAKOTAIAH, V. 2000 Experimental study of wave occlusion on falling films in a vertical pipe. *AIChE J.* **46** (7), 1300–1306.
- DELAUNAY, C. 1841 Sur la surface de révolution dont la courbure moyenne est constante. *J. Math. Pures Appl.* **6**, 309–320.
- DIETZE, G.F. 2022 Falling Liquid Films in narrow geometries and other Thin Film Flows. Habilitation thesis, Université Paris-Saclay, HAL Id tel-04437816.
- DIETZE, G.F., LAVALLE, G. & RUYER-QUIL, C. 2020 Falling liquid films in narrow tubes: occlusion scenarios. *J. Fluid Mech.* **894**, A17.
- DIETZE, G.F. & RUYER-QUIL, C. 2015 Films in narrow tubes. *J. Fluid Mech.* **762**, 68–109.
- DING, Z., LIU, Z., LIU, R. & YANG, C. 2019 Thermocapillary effect on the dynamics of liquid films coating the interior surface of a tube. *Intl J. Heat Mass Transfer* **138**, 524–533.
- DOEDEL, E.J. 2008 AUTO07P: *Continuation and Bifurcation Software for Ordinary Differential Equations*. Montreal Concordia University.
- EVERETT, D.H. & HAYNES, J.M. 1972 Model studies of capillary condensation. *J. Colloid Interface Sci.* **38** (1), 125–137.
- FAHY, J.V. & DICKEY, B.F. 2010 Airway mucus function and dysfunction. *New England J. Med.* **363** (23), 2233–2247.
- FILOCHE, M., TAI, C.-F. & GROTERBERG, J.B. 2015 Three-dimensional model of surfactant replacement therapy. *Proc. Natl Acad. Sci. USA* **112** (30), 9287–9292.
- FUJIOKA, H. & GROTERBERG, J.B. 2004 Steady propagation of a liquid plug in a two-dimensional channel. *J. Biomech. Engng* **126** (5), 567–577.
- FUJIOKA, H., HALPERN, D., RYANS, J. & GAVER III, D.P. 2016 Reduced-dimension model of liquid plug propagation in tubes. *Phys. Rev. Fluids* **1**, 053201.
- FUJIOKA, H., TAKAYAMA, S. & GROTERBERG, J.B. 2008 Unsteady propagation of a liquid plug in a liquid-lined straight tube. *Phys. Fluids* **20** (6), 062104.
- GROTERBERG, J. 1994 Pulmonary flow and transport phenomena. *J. Fluid Mech.* **26**, 529–571.
- GROTERBERG, J. 2011 Respiratory fluid mechanics. *Phys. Fluids* **23**, 021301.
- HALPERN, D., JENSEN, O.E. & GROTERBERG, J.B. 1998 A theoretical study of surfactant and liquid delivery into the lung. *J. Appl. Physiol.* **85**, 333–352.
- HASSAN, E.A., UZGOREN, E., FUJIOKA, H., GROTERBERG, J.B. & SHYY, W. 2011 Adaptive Lagrangian–Eulerian computation of propagation and rupture of a liquid plug in a tube. *Intl J. Numer. Meth. Fluids* **67** (11), 1373–1392.
- HEIL, M. 2001 Finite Reynolds number effects in the Bretherton problem. *Phys. Fluids* **13** (9), 2517–2521.
- HICKOX, C.E. 1971 Instability due to viscosity and density stratification in axisymmetric pipe flow. *Phys. Fluids* **14** (2), 251–262.
- HOGG, J.C. 2006 State of the art. Bronchiolitis in chronic obstructive pulmonary disease. *Proc. Am. Thor. Soc.* **3** (6), 489–493.
- HOWELL, P.D., WATER, S.L. & GROTERBERG, J.B. 2000 The propagation of a liquid bolus along a liquid-lined flexible tube. *J. Fluid Mech.* **406**, 309–335.
- HU, Y., BIAN, S., GROTERBERG, J., FILOCHE, M., WHITE, M., TAKAYAMA, J. & GROTERBERG, J.B. 2015 A microfluidic model to study fluid dynamics of mucus plug rupture in small lung airways. *Biomicrofluidics* **9** (4), 044119.

- HU, Y., ROMANO, F. & GROTBORG, J.B. 2020 Effects of surface tension and yield stress on mucus plug rupture: a numerical study. *J. Biomech. Engng* **142** (6), 061007.
- HUH, D., FUJIOKA, H., TUNG, Y.-C., FUTAI, N., PAINE, R., GROTBORG, J.B. & TAKAYAMA, S. 2007 Acoustically detectable cellular-level lung injury induced by fluid mechanical stresses in microfluidic airway systems. *Proc. Natl Acad. Sci. USA* **104** (48), 18886–18891.
- JENSEN, M.H., LIBCHABER, A., PELCE, P. & ZOCCHI, G. 1987 Effect of gravity on the Saffman–Taylor meniscus: theory and experiment. *Phys. Rev. A* **35**, 2221.
- KALLIADASIS, S. & CHANG, H.-C. 1994 Apparent dynamic contact angle of an advancing gas-liquid meniscus. *Phys. Fluids* **6** (1), 12–23.
- KALLIADASIS, S., RUYER-QUIL, C., SCHEID, B. & VELARDE, M.G. 2012 *Falling Liquid Films*. Applied Mathematical Sciences, vol. 176. Springer.
- KAY, S.S., BILEK, A.M., DEE, K.C. & GAVR III, D.P. 2004 Pressure gradient, not exposure duration, determines the extent of epithelial cell damage in a model of pulmonary airway reopening. *J. Appl. Physiol.* **97**, 269–352.
- KHODAPARAST, S., KIM, M.K., SILPE, J.E. & STONE, H.A. 2017 Bubble-driven detachment of bacteria from confined microgeometries. *Environ. Sci. Technol.* **51** (3), 1340–1347.
- KLASEBOER, E., GUPTA, R. & MANICA, R. 2014 An extended Bretherton model for long Taylor bubbles at moderate capillary numbers. *Phys. Fluids* **26**, 032107.
- LAMSTAES, C. & EGGERS, J. 2017 Arrested bubble rise in a narrow tube. *J. Stat. Phys.* **167**, 656–682.
- LASSEUX, D. 1995 Drainage in a capillary: a complete approximated description of the interface. *C. R. Acad. Sci. Ser. Iib* **321**, 125–131.
- MAGNIEZ, J.C., BAUDOIN, M., LIU, C. & ZOUESHTIAGH, F. 2016 Dynamics of liquid plugs in prewetted capillary tubes: from acceleration and rupture to deceleration and airway obstruction. *Soft Matt.* **12**, 8710–8717.
- MAMBA, S.S., MAGNIEZ, J.C., ZOUESHTIAGH, F. & BAUDOIN, M. 2018 Dynamics of a liquid plug in a capillary tube under cyclic forcing: memory effects and airway reopening. *J. Fluid Mech.* **838**, 165–191.
- MAMBA, S.S., ZOUESHTIAGH, F. & BAUDOIN, M. 2019 Pressure-driven dynamics of liquid plugs in rectangular microchannels: influence of the transition between quasi-static and dynamic film deposition regimes. *Intl J. Multiphase Flow* **113**, 343–357.
- MATHEMATICA 2014 *Version 10.0.2.0*. Wolfram Research.
- MURADOGLU, M., ROMANO, F., FUJIOKA, H. & GROTBORG, J.B. 2019 Effects of surfactant on propagation and rupture of a liquid plug in a tube. *J. Fluid Mech.* **872**, 407–437.
- NAVON, I.M. 1987 PENT: a periodic pentadiagonal systems solver. *Commun. Appl. Numer. Meth.* **3**, 63–69.
- NIKOLAYEV, V.S. & MARENGO, M. 2018 Pulsating heat pipes: basics of functioning and modeling. In *ENCYCLOPEDIA OF TWO-PHASE HEAT TRANSFER AND FLOW IV: Modeling Methodologies, Boiling of CO<sub>2</sub>, and Micro-Two-Phase Cooling Volume 1: Modeling of Two-Phase Flows and Heat Transfer* (ed. J.R. Thome), pp. 63–139. World Scientific.
- OGROSKY, H.R. 2021a Impact of viscosity ratio on falling two-layer viscous film flow inside a tube. *Phys. Rev. Fluids* **6**, 104005.
- OGROSKY, H.R. 2021b Linear stability and nonlinear dynamics in a long-wave model of film flows inside a tube in the presence of surfactant. *J. Fluid Mech.* **908**, A23.
- OLGAC, U. & MURADOGLU, M. 2013 Computational modeling of unsteady surfactant-laden liquid plug propagation in neonatal airways. *Phys. Fluids* **25** (7), 071901.
- PARK, C.-W. & HOMSY, G.M. 1984 Two-phase displacement in hele shaw cells: theory. *J. Fluid Mech.* **139**, 291–308.
- PATANKAR, S.V. 1980 *Numerical Heat Transfer and Fluid Flow*. Taylor & Francis.
- PIROIRD, K., CLANET, C. & QUÉRÉ, D. 2011 Detergency in a tube. *Soft Matt.* **7**, 7498–7503.
- POPINET, S. 2009 An accurate adaptive solver for surface-tension-driven interfacial flows. *J. Comput. Phys.* **228**, 5838–5866.
- RICHARD, G., RUYER-QUIL, C. & VILA, J.P. 2016 A three-equation model for thin films down an inclined plane. *J. Fluid Mech.* **804**, 162–200.
- ROMANO, F., MURADOGLU, M., FUJIOKA, H. & GROTBORG, J.B. 2021 The effect of viscoelasticity in an airway closure model. *J. Fluid Mech.* **913**, A31.
- RYANS, J., FUJIOKA, H., HALPERN, D. & GAVR III, D.P. 2016 Reduced-dimension modeling approach for simulating recruitment/de-recruitment dynamics in the lung. *Ann. Biomed. Engng* **44**, 3619–3631.
- SPAGNOLIE, S.E. (Ed.) 2015 *Complex Fluids in Biological Systems – Experiment, Theory, and Computation*. Springer.
- SRINIVASAN, V., RAHATGAONKAR, A.M. & KHANDEKAR, S. 2021 Hydrodynamics of a completely wetting isolated liquid plug oscillating inside a square capillary tube. *Intl J. Multiphase Flow* **135**, 103534.

## *Liquid plugs in narrow tubes*

- SURESH, V. & GROTBORG, J.B. 2005 The effect of gravity on liquid plug propagation in a two-dimensional channel. *Phys. Fluids* **17** (3), 031507.
- TAVANA, H., KUO, C.-H., LEE, Q.Y., MOSADEGH, B., HUH, D., CHRISTENSEN, P.J., GROTBORG, J.B. & TAKAYAMA, S. 2010 Dynamics of liquid plugs of buffer and surfactant solutions in a micro-engineered pulmonary airway model. *Langmuir* **26** (5), 3744–3752.
- TAVANA, H., ZAMANKHAN, P., CHRISTENSEN, P.J., GROTBORG, J.B. & TAKAYAMA, S. 2011 Epithelium damage and protection during reopening of occluded airways in a physiologic microfluidic pulmonary airway model. *Biomed. Microdevices* **13** (4), 731–742.
- TAYLOR, G.I. 1961 Deposition of a viscous fluid on the wall of a tube. *J. Fluid Mech.* **10** (2), 161–165.
- THIELE, U., VELARDE, M.G., NEUFFER, K & POMEAU, Y. 2001 Sliding drops in the diffuse interface model coupled to hydrodynamics. *Phys. Rev. E* **64** (6), 061601.
- UBAL, S., CAMPANA, D.M., GIAVEDONI, M.D. & SAITA, F.A. 2008 Stability of the steady-state displacement of a liquid plug driven by a constant pressure difference along a prewetted capillary tube. *Ind. Engng Chem. Res.* **47**, 6307–6315.
- VASQUEZ, P.A., JIN, Y., PALMER, E., HILL, D. & FOREST, M.G. 2016 Modeling and simulation of mucus flow in human bronchial epithelial cell cultures. Part I. Idealized axisymmetric swirling flow. *PLoS Comput. Biol.* **12** (8), e1004872.
- WEBER, J., STRAKA, L., BORGMANN, S., SCHMIDT, J., WIRTH, S. & SCHUMANN, S. 2020 Flow-controlled ventilation (fcv) improves regional ventilation in obese patients—a randomized controlled crossover trial. *BMC Anesthesiol.* **20**, 1–10.
- WEIBEL, E.R. & GOMEZ, D.M. 1962 Architecture of the human lung: use of quantitative methods establishes fundamental relations between size and number of lung structures. *Science* **137** (3530), 577–585.
- YU, Y.E., KHODAPARAST, S. & STONE, H.A. 2018 Separation of particles by size from a suspension using the motion of a confined bubble. *Appl. Phys. Lett.* **112**, 181604.
- ZHENG, Y., FUJIOKA, H. & GROTBORG, J.B. 2007 Effects of gravity, inertia, and surfactant on steady plug propagation in a two-dimensional channel. *Phys. Fluids* **19** (8), 082107.
- ZOUESHTIAGH, F., BAUDOIN, M. & GUERRIN, D. 2014 Capillary tube wetting induced by particles: towards armoured bubbles tailoring. *Soft Matt.* **10**, 9403–9412.